AGU PUBLICATIONS

JGR

Journal of Geophysical Research: Oceans

RESEARCH ARTICLE

10.1002/2014JC010097

The imprint of Southern Ocean overturning on seasonal water mass variability in Drake Passage

Dafydd Gwyn Evans[1], **Jan D. Zika**[1], **Alberto C. Naveira Garabato**[1], and **A. J. George Nurser**[2]

[1]Ocean and Earth Science, National Oceanography Centre Southampton, University of Southampton, Southampton, UK,
[2]National Oceanography Centre, University of Southampton Waterfront Campus, European Way, Southampton, UK

Key Points:
- Seasonal variability of Southern Ocean water masses observed in Drake Passage
- Overturning in Drake Passage resolved in thermohaline coordinates
- Balance between wind-driven overturning and seasonal water mass transformation

Correspondence to:
D. G. Evans,
dafydd.evans@noc.soton.ac.uk

Citation:
Evans, D. G., J. D. Zika, A. C. N. Garabato, and A. J. G. Nurser (2014), The imprint of Southern Ocean overturning on seasonal water mass variability in Drake Passage, *J. Geophys. Res. Oceans*, *119*, 7987–8010, doi:10.1002/2014JC010097.

Received 29 APR 2014
Accepted 26 OCT 2014
Accepted article online 31 OCT 2014
Published online 25 NOV 2014

Abstract Seasonal changes in water mass properties are discussed in thermohaline coordinates from a seasonal climatology and repeat hydrographic sections. The SR1b CTD transects along Drake Passage are used as a case study. The amount of water within temperature and salinity classes and changes therein are used to estimate dia-thermal and dia-haline transformations. These transformations are considered in combination with climatologies of surface buoyancy flux to determine the relative contributions of surface buoyancy fluxes and subsurface mixing to changes in the distribution of water in thermohaline coordinates. The framework developed provides unique insights into the thermohaline circulation of the water masses that are present within Drake Passage, including the erosion of Antarctic Winter Water (AAWW) during the summer months and the interaction between the Circumpolar Deep Waters (CDW) and Antarctic Intermediate Water (AAIW). The results presented are consistent with summertime wind-driven inflation of the CDW layer and deflation of the AAIW layer, and with new AAIW produced in the winter as a mixture of CDW, remnant AAWW, and surface waters. This analysis therefore highlights the role of surface buoyancy fluxes in the Southern Ocean overturning.

1. Introduction

The temperature and salinity of the ocean change on a broad spectrum of temporal and spatial scales [*Bindoff and McDougall*, 1994; *Bryden et al*., 2003; *Delcroix et al*., 2005]. Such changes are associated with both diabatic (e.g., buoyancy fluxes) and adiabatic (e.g., isopycnal heaving) processes. Diagnosing what drives both intraannual and decadal fluctuations is crucial for understanding the variations of temperature and salinity observed on regional [*Delcroix et al*., 1996; *Curry et al*., 1998, 2003; *Meijers et al*., 2011] and global [*Durack and Wijffels*, 2010; *Purkey and Johnson*, 2010; *Durack et al*., 2012] scales.

Observed from a conventional Eulerian (fixed geographic) perspective, the ocean is subject to both diabatic and adiabatic changes in temperature and salinity. That is, from a hydrographic record of a particular location in the ocean, one may observe a diabatic change over time in temperature or salinity that is the consequence of variations in the balance of surface heat fluxes or evaporation minus precipitation ($E - P$) at the region of the surface ocean in which the observed water type is formed, or variations in the strength of mixing processes. In addition, the same fixed hydrographic record is influenced by adiabatic heaving of isopycnals on both seasonal [e.g., *Chelton et al*., 2011] and interannual [*Boning et al*., 2008] time scales. These do not represent an addition/removal of freshwater or heat at the surface ocean. Thus, when attempting to understand the variability in the ocean, isolating the diabatic contribution is crucial.

Observing the ocean from an isopycnal framework removes changes due to isopycnal heaving [*Bindoff and McDougall*, 1994]. Effective use of this method, however, must be underpinned by a robust understanding of how variability in surface ocean fluxes of freshwater and heat are translated onto observations from an isopycnal perspective. *Bindoff and McDougall* [1994] separate the above changes in the ocean into three scenarios: pure warming, pure freshening, and pure heave, presenting the resultant difference from both pressure and isopycnal perspectives. They highlight the counterintuitive nature of temperature and salinity change on isopycnals. Assuming temperature and salinity decrease with depth, a warming at fixed depth is reflected as a cooling and freshening on an isopycnal. However, a freshening at fixed depth also manifests as a freshening and a cooling on an isopycnal.

Durack and Wijffels [2010] demonstrate the importance of considering the effect of the meridional migration of isopycnal outcrops on changes observed on isopycnal surfaces. These processes will project as changes on isopycnals, for example, as isopycnal outcrops migrate due to large-scale warming of the ocean, through the mean salinity field set by the stationary $E - P$ field. This would produce an adiabatic change in salinity on isopycnal surfaces that does not reflect a change in the global freshwater budget.

Isopycnal outcrop and frontal migration may also occur as a result of dynamical processes. An alternative method to assess changes on isopycnal surfaces was utilized in the Southern Ocean by remotely tracking the position of dynamic height contours [*Meijers et al*., 2011]. *Meijers et al*. [2011] show an adiabatic warming across the Antarctic Circumpolar Current (ACC) induced by the wind-driven poleward migration of isopycnal outcrops. The usefulness of this method is restricted by the assumption that temperature and salinity profiles are uniquely zonally coherent.

An alternative to density or dynamic height coordinates is to project observations into thermohaline (temperature versus salinity) coordinates. Again, this naturally removes the effect of isopycnal heaving. *Bryden et al*. [2003], for example, used this method to assess decadal water mass changes by estimating the minimum change between two profiles in thermohaline coordinates. They showed patterns of coherent change between transects across the Indian Ocean. Such methods are still, however, subject to the adiabatic process of frontal migration.

Quantitative methods first developed by *Walin* [1982] have been used to investigate changes in water mass coordinates. Fluxes in water mass coordinates are assessed in terms of air-sea fluxes and diapycnal mixing, integrated across water mass volumes defined by their temperature or density [*Nurser et al*., 1999; *Grist et al*., 2009; *Maze et al*., 2009; *Cerovečki et al*., 2011; *Badin et al*., 2013], thus naturally following frontal boundaries. These methods have been extended to thermohaline coordinates (i.e., two tracers) to understand surface fluxes [*Speer*, 1993], the global thermohaline circulation [*Döös et al*., 2012; *Zika et al*., 2012] and the role of variability in that circulation [*Groeskamp et al*., 2014]. However, no study has yet applied the water mass transformation framework to understand changes in observations in thermohaline coordinates. Such methods incorporate the best of both the isopycnal framework and the tracking of frontal movements, as following water masses defined by their temperature and salinity implicitly follows isopycnal movement both vertically and horizontally. In addition, changes within thermohaline coordinates are more natural than changes within an isopycnal framework (i.e., the pure warming and pure freshening scenarios of *Bindoff and McDougall* [1994]) and the geographically distinct thermohaline properties of water masses enable a global analysis within thermohaline coordinates.

The importance of understanding water mass changes in the Southern Ocean is underscored by the fact that the ACC plays a key role in the transformation, formation, and ventilation of the world's water masses [*Rintoul and Naveira-Garabato*, 2013; *Talley*, 2013]. Thus, it is important to understand the sensitivity of the ACC to the changes in the surface buoyancy fluxes and extratropical southern hemisphere westerlies projected for the 21st century [*Fyfe and Saenko*, 2006; *Downes et al*., 2009]. Within Drake Passage, the focus for this study, and the South Atlantic region as a whole, a balance between surface buoyancy fluxes, wind-driven Ekman transport and upwelling, interior diapycnal mixing and eddy stirring/advection controls the distribution of water masses [*Speer et al*., 2000; *Naveira Garabato et al*., 2007; *Zika et al*., 2009; *Marshall and Speer*, 2012]. In particular, this includes the upwelling and transformation of North Atlantic Deep Water (NADW) into the Upper and Lower Circumpolar Deep Waters (UCDW/LCDW), the formation and export of Antarctic Bottom Water (AABW), subduction of Antarctic Intermediate Water (AAIW) and Sub-Antarctic Mode Water (SAMW), and the seasonal formation and erosion of Antarctic Winter Water (AAWW; see the two top left plots of Figure 1 for the geographical locations of each water mass along a transect across Drake Passage). The role of seasonal changes in the air-ice-sea buoyancy fluxes of heat and freshwater in the formation of these water masses is less clear.

This study combines and expands on the work of *Walin* [1982] and *Speer* [1993] to explore the seasonal water mass changes in terms of volumes of water in thermohaline coordinates from a repeat hydrographic transect along Drake Passage. We estimate dia-surface water mass transformations as fluxes across isotherms and isohalines, and use these estimates in combination with dia-surface transformations inferred from sea-surface heat and freshwater fluxes to describe the diabatic processes responsible for

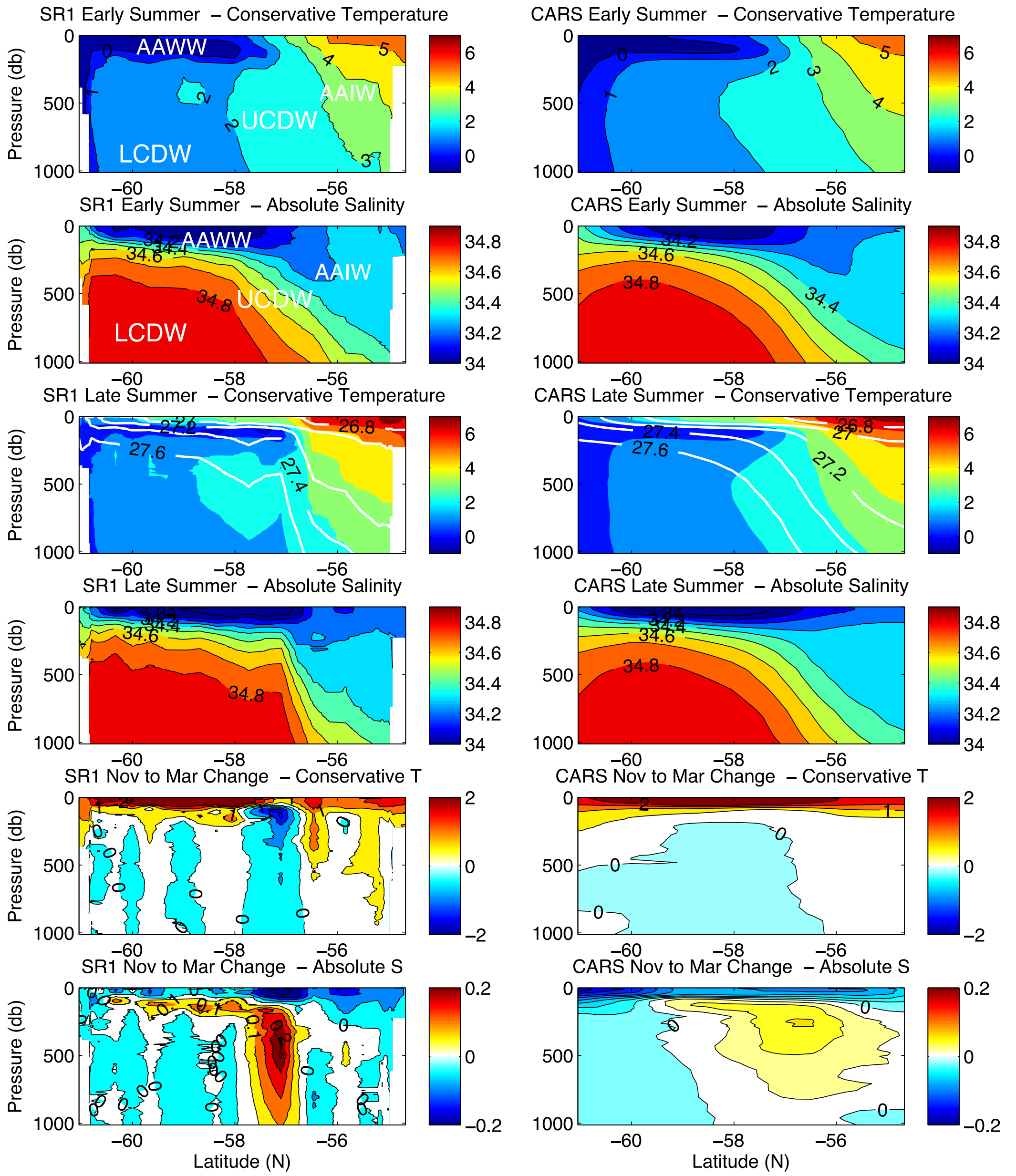

Figure 1. (left column) Mean early summer and late summer section comparison of Θ and *S* from the SR1b section occupations and (right column) the CARS seasonal climatology. White contours are potential density anomaly referenced to zero pressure. Labels show Antarctic Winter Water (AAWW), Antarctic Intermediate Water (AAIW), Upper Circumpolar Deep Water (UDCW), and Lower Circumpolar Deep Water (LCDW). The bottom two plots of each figure are the mean late summer section minus the mean early summer section.

changes in the distribution of water in thermohaline coordinates. Exploring well-defined seasonal changes in this way enables a clearer understanding of the advantages and disadvantages of this technique, which will be useful for the exploration of longer term (interannual and beyond) trends in temperature and salinity.

Using this water mass transformation framework, we resolve the upwelling (CDW) and downwelling (AAIW/SAMW) limbs of the Southern Ocean overturning circulation enabled by the seasonal changes of buoyancy exchange between the atmosphere and the ocean. In the next section, we describe the data that we use and our method for the calculation of dia-surface water mass transformations. Sections 3 and 4 describe seasonal changes along Drake Passage in Eulerian and thermohaline coordinates and in section 6 we project the changes calculated in thermohaline coordinates into Eulerian coordinates. These results are interpreted in section 7 and summarized in section 8.

2. Methods

2.1. Data

This study uses conservative temperature (Θ) and absolute salinity (*S*) calculated from two different observational data sets: shipboard conductivity-temperature-depth (CTD) sections and a hydrographic climatology. The shipboard CTD data comprises 20 repeat transects along Drake Passage SR1b sections, occupied between November 1993 and March 2013, available online from the British Oceanographic Data Centre (www.bodc.ac.uk). The advantages of Θ and *S* over potential temperature and practical salinity are discussed in *IOC et al*. [2010]. The data are near-bottom 2 db resolution profiles of Θ, *S*, and pressure from stations separated on average by ∼20 nautical miles, between 54.67°S and 61.05°S and at 56.56°W. The occupations we use are between November and March, with the majority occurring during December. As a result, our analysis performed using the SR1b data set is restricted to a comparison between early and late summer. Some transects are incomplete and are not used as part of this analysis.

To augment this approach, we also use the CSIRO Atlas of Regional Seas (CARS) 2009. This global climatology provides an atlas of seasonal water mass properties at a 1/2° resolution derived from all available historical subsurface measurements [*Ridgway et al*., 2002], including CTD data from 1972 within Drake Passage. The data were accessed at www.cmar.csiro.au/cars, from which Θ and *S* sections replicating the SR1b nominal stations were extracted for comparison with seasonal changes in the SR1b transects. The CARS climatology is restricted to the surface 1000 m, so analysis of the SR1b section data will also be restricted to this depth. The CARS climatology includes year-round estimates of seasonal mean temperature and salinity constructed from a mean state estimate and the annual and semiannual harmonic components. This enables both a comparison with the summer changes derived from the SR1b data and further analysis into seasonal changes during the austral winter.

The variability within the SR1b section data is typically dominated by mesoscale processes, apparent as an adiabatic heaving of isopycnals (e.g. compare slope of white contours from SR1b and CARS in Figure 1). This makes changes between occupations difficult to interpret. Due to the idealized nature of the fitted seasonal cycle and the lower vertical and horizontal resolution, this is not the case within the CARS seasonal climatology. Therefore, one of the main goals for this study is to compare these data sets, and to assess whether or not we can resolve the same seasonal changes in both data sets, by removing this aliased adiabatic mesoscale variability from the seasonal changes observed in the section occupations. That much of the CARS seasonal climatology is likely constructed using SR1b data in this region should not affect the outcome of this analysis given our aim to simply remove the aliased mesoscale variability present in the SR1b data. The CARS seasonal climatology otherwise mostly uses data from Argo profiling floats, particularly during the winter.

We utilize two global air/sea flux climatologies for the sake of comparison: the NOCS flux V2.0 [*Berry and Kent*, 2009] and a combination of the Woods Hole Oceanographic Institute (WHOI) OAflux/International Satellite Cloud Climatology Project (ISCCP)/Global Precipitation Climatology Project (GPCP) data sets [*Yu et al*., 2006]. From the WHOI OAflux project (hereinafter WHOI; accessed from http://oaflux.whoi.edu) the net heat flux and evaporation products are used. The data used are monthly mean values, globally gridded to 1° for the period 1958–present. The net heat flux data set is a combination of WHOI products and ISCCP radiation products [*Schiffer and Rossow*, 1985; hosted on the WHOI OAflux project website]. Using the WHOI data set, freshwater fluxes are determined through a combination of the WHOI evaporation product and monthly mean precipitation data from the GPCP. This combines various satellite and gauge measurements of precipitation into a merged 2.5° global data set [*Adler et al*., 2003]. The NOCS flux V2.0 data set (hereinafter NOCSv2) is described in Appendix A. For both the products, data are limited during the winter at the southern end of the transect due to sea-ice cover. Data from all surface flux data sets are linearly interpolated onto the station positions associated with the SR1b section.

2.2. Dia-Tracer Transformation Calculation

The following section describes a general method to represent changes of Θ and *S* in the ocean as dia-thermal and dia-haline transformations of water between water mass classes in thermohaline coordinates. These dia-surface transformations should be interpreted as volume fluxes of water and have units of m^3 s^{-1}. They cannot be practically diagnosed from velocity measurements and must therefore be determined indirectly from changes in the volumetric distribution of water projected into thermohaline coordinates. In the case of a two-dimensional ocean transect, which is the focus for this analysis, the method is identical; however, the inferred transformations are area fluxes and have units of $\mathrm{m}^2\ \mathrm{s}^{-1}$.

To infer these dia-surface transformations, first consider the conservation of some tracer, C, which, assuming incompressible flow, can be described as follows:

$$\frac{\partial C}{\partial t}+\mathbf{u}\cdot\nabla C=f_C+\nabla\cdot\mathbf{K}\nabla C. \tag{1}$$

Here $\mathbf{u}$ is the three-dimensional Eulerian velocity, f_C is a source/sink of C and $\mathbf{K}$ is a diffusion tensor encompassing both the isopycnal and diapycnal mixing coefficients. Here the change in C is separated into the Eulerian and advective components (LHS), which are balanced by a diabatic flux term and a diffusive term (RHS).

Dividing the left-hand side of equation (1) by the modulus of the tracer gradient gives the dia-surface velocity component (u_C), the component of the velocity that crosses the surface of constant C, so that:

$$u_C=\frac{1}{|\nabla C|}\frac{\partial C}{\partial t}+\mathbf{u}\cdot\frac{\nabla C}{|\nabla C|}. \tag{2}$$

Here $(\partial C/\partial t)/|\nabla C|$ is the component of the dia-surface velocity due to movement of the surface of constant C and $(\mathbf{u}\cdot\nabla C)/|\nabla C|$ is the component of the dia-surface velocity due to Eulerian flow normal to the surface of constant C. Note u_C has units of $\mathrm{m\ s}^{-1}$. Equation (2) will be undefined where $|\nabla C|=0$ but no isosurface will exist there either. We now consider the tracers Θ and S, so that u_{Θ^*} becomes the dia-thermal velocity crossing the isotherm Θ and u_{S^*} the dia-haline velocity crossing the isohaline S. The transformation across each isotherm (Θ) within the salinity class $S^*=S\pm\Delta S/2$ and across the isohaline (S) within the temperature range $\Theta^*=\Theta\pm\Delta\Theta/2$ will, therefore, be:

$$U_\Theta(\Theta,S)=\int_{\Theta^*=\Theta}\Pi(S,S^*)u_{\Theta^*}\,\mathrm{d}A, \tag{3}$$

$$U_S(\Theta,S)=\int_{S^*=S}\Pi(\Theta,\Theta^*)u_{S^*}\,\mathrm{d}A, \tag{4}$$

where Π is a boxcar function that is 0 when Θ or S is outside the range defined by the given Θ-S class, or 1 when Θ and S are within this range, while $\int \mathrm{d}A$ is an integral over the surface area of the isotherm within the salinity limits or over the isohaline surface within the temperature limits. A positive transformation represents water moving to warmer and saltier water mass classes. Thus, the rate of change of a volume of water defined by a given Θ-S class ($\Theta^*=\Theta\pm\Delta\Theta/2, S^*=S\pm\Delta S/2$) in terms of the transformation of water across isotherms and isohalines defined at $\Theta\pm\Delta\Theta/2$ and $S\pm\Delta S/2$ is

$$\begin{aligned}\left.\frac{DV}{Dt}\right|_{\Theta,S}&=U_\Theta(\Theta-\Delta\Theta/2,S)-U_\Theta(\Theta+\Delta\Theta/2,S)\\&+U_S(\Theta,S-\Delta S/2)-U_S(\Theta,S+\Delta S/2)+\epsilon(\Theta,S).\end{aligned} \tag{5}$$

This relation is shown schematically in Figure 2 in both geographical coordinates (top) and thermohaline coordinates (bottom). Here the volume of water at Θ and S is set by the transformation of water across the isotherms $\Theta-\Delta\Theta/2$ and $\Theta+\Delta\Theta/2$, and the isohalines $S-\Delta S/2$ and $S+\Delta S/2$, with dia-surface transformations of $U_\Theta(\Theta-\Delta\Theta/2,S)$, $U_\Theta(\Theta+\Delta\Theta/2,S)$, $U_S(\Theta,S-\Delta S/2)$, and $U_S(\Theta,S+\Delta S/2)$, respectively, as given in (5). These dia-surface transformations therefore represent the volume of water transformed per unit time by $\Delta\Theta$ for the dia-thermal components and by ΔS for the dia-haline components, to account for the volume change within each Θ-S class. Volume fluxes into and out of the geographical domain within which thermohaline volumes are determined may be interpreted as two additional unknown volume flux terms on the RHS of equation (5), which have been combined into ϵ.

The dia-surface transformations across each isotherm and isohaline are thus constrained by the volume changes of each Θ-S class. We can then uniquely determine the dia-surface transformations by solving for the transformation field with minimum magnitude that satisfies equation (5). The volume changes are determined as follows. First, a nominal grid spacing in thermohaline coordinates is chosen. This grid spacing must be fine enough to resolve the finer water mass transformations in the specified region, but coarse

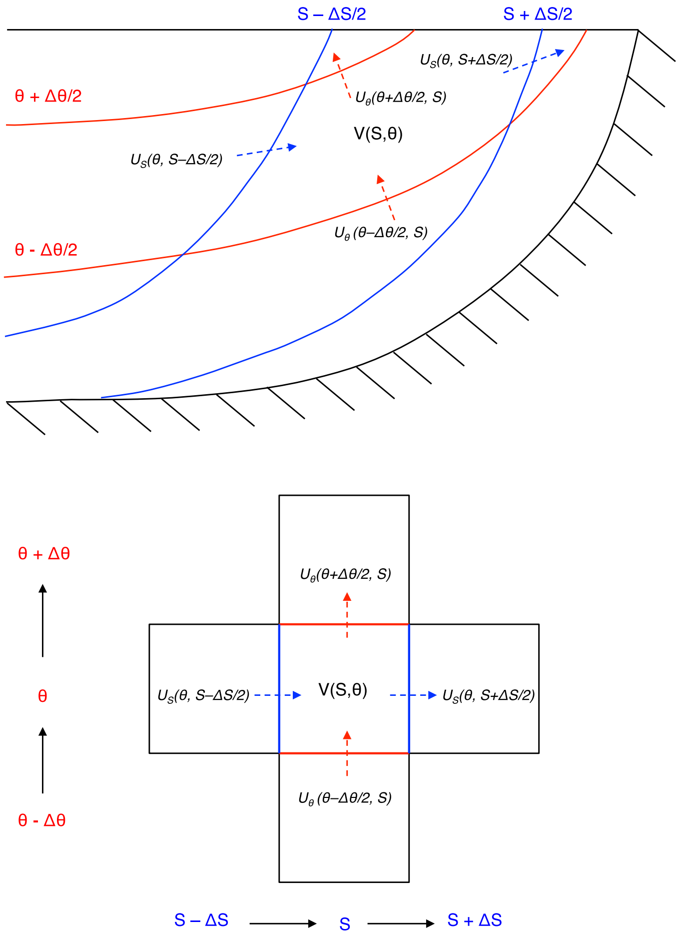

Figure 2. Schematic of the relation described by (5) for a given value of Θ and *S*.

enough to give adequate coverage in Θ-*S* coordinates so that there are not any artificially disconnected regions separated by no data. Further, it is advantageous to choose Θ and *S* spacings that have a roughly similar contribution in terms of changes in density. A resolution of 0.25°C and 0.025 g kg^{-1} is chosen to meet these criteria. As would be expected, a coarser resolution in Θ and *S* gives larger individual volumes and thus larger dia-surface transformations as in general the total volume should not increase.

To calculate the water mass volume associated with each Θ-*S* class, the volume of each geographical grid cell was calculated (i.e., zonal × meridional × vertical extent, or meridional × vertical extent for an ocean section). The Θ-*S* value at the center of each geographical grid cell was determined through linear interpolation. The thermohaline volume for a given Θ-*S* class is then the sum of the volume associated with each geographical grid cell within the range $\Theta \pm \Delta\Theta/2$ and $S \pm \Delta S/2$. In practice, for this study the thermohaline area associated with each SR1 section occupation is normalized so that the total area of each section is the same. Note that a particular Θ-*S* combination can exist in multiple locations within the geographical grid, for example, by advection by eddies. An advantage of this method is its ability to capture the effect that such processes have on these water masses. Further, by definition water masses in adjacent Θ-*S* classes must be adjacent in geographical coordinates as there cannot be a discrete jump in the gradient of Θ or *S*, unless separated by a land mass, which is not the case in this study.

Using (5), a set of linear equations can be built to link the observed change in volume of each Θ-*S* class, as determined above, to the dia-surface transformations within the defined thermohaline coordinate space:

$$\mathbf{Ax}=\mathbf{b}, \tag{6}$$

where

$$\mathbf{A}=\begin{bmatrix} -1 & 0 & \cdots & 0 & -1 & \cdots & 0 & 0 & \cdots & 0 \\ 1 & -1 & \cdots & 0 & 0 & \cdots & 0 & 1 & \cdots & 0 \\ \vdots & \vdots & \ddots & \vdots & \vdots & \ddots & \vdots & \vdots & \ddots & \vdots \\ 0 & 0 & \cdots & 1 & 0 & \cdots & 1 & 0 & \cdots & 0 \end{bmatrix}, \tag{7}$$

$$\mathbf{b}=\left[\left.\frac{DV}{Dt}\right|_{\Theta_1,S_1}, \left.\frac{DV}{Dt}\right|_{\Theta_2,S_1}, \ldots, \left.\frac{DV}{Dt}\right|_{\Theta_m,S_n}\right], \tag{8}$$

$$\begin{aligned}\mathbf{x}=&[U_\Theta((\Theta_2+\Theta_1)/2,S_1),U_\Theta((\Theta_3+\Theta_2)/2,S_1),\ldots,U_\Theta((\Theta_m+\Theta_{(m-1)})/2,S_n),\\&U_S(\Theta_1,(S_2+S_1)/2),U_S(\Theta_2,(S_2+S_1)/2)),\ldots,U_S(\Theta_m,(S_n+S_{(n-1)})/2),\\&\epsilon(\Theta_1,S_1),\ldots,\epsilon(\Theta_m,S_n)]n.\end{aligned}\tag{9}$$

Here the vector **b** is the observed change in volume of each Θ-S class, divided by the relevant time-interval and should be $m\times n$ long, where m is the number of individual Θ classes and n is the number of individual S classes. The vector of unknowns **x** will therefore be the dia-thermal and dia-haline transformations and the volume change associated with ϵ. The vector **x** will have length $[(m-1)\times n]+[m\times(n-1)]+(m\times n)$. The matrix **A** represents the coefficients relating each term on the RHS of (5) to the volume change. Each of the $m\times n$ rows represents the equation for the change in volume of a Θ-S class. The first $[(m-1)\times n]+[m\times(n-1)]$ columns in **A** correspond to each Θ or S iso-surface, and the coefficients describe the relation of each iso-surface to the Θ-S class designated in each row. A coefficient of 1 is assigned to the isotherm (or isohaline) at $\Theta-\Delta\Theta/2$, and a coefficient of -1 is assigned to the isotherm (or isohaline) at $\Theta+\Delta\Theta/2$. The coefficient is zero for each isotherm and isohaline that is not adjacent in thermohaline coordinates to the Θ-S class associated with the given row.

The last $m\times n$ columns of **A** represent each Θ-S class, to which a coefficient of 1 is assigned if that value of Θ or S is adjacent to the boundary of the domain in geographical coordinates; thus allowing a flux into or out of the domain due to the terms combined into ϵ. Further, we are assuming that only advection meridionally through the northern boundary of the geographical domain will affect the distribution of volume in thermohaline coordinates. The linear equations can then be solved for **x** using a least squares regression, where the sum of the squared residuals ($\mathbf{b}-\mathbf{Ax}$) are minimized. For all calculations, the relative residuals ($(|\mathbf{b}-\mathbf{Ax}|)/|\mathbf{b}|$) are less than 0.001 and generally $<1\times10^{-6}$. The derived transformations, therefore, represent the minimum combination of volume fluxes required to explain the volume change of each Θ-S class.

The temporal distribution of SR1b section occupations enables analysis of the changes in water mass area and the associated dia-surface transformation from early to late summer. The early summer water mass area is estimated from five November section occupations (1993, 1994, 1996, 2000, and 2001) by calculating the water mass area in Θ-S space for each individual section and computing the mean area. The late summer estimate is determined in the same way from three section occupations from February 2000, February 2009, and March 2013. The seasonal change in water mass area distribution is, therefore, the difference between early and late summer. This change divided by the time-interval from early to late summer (3.5 months) is used to populate **b** and thus infer the seasonal fluxes of water mass area. The early to late summer water mass area changes and inferred dia-surface transformations are not sensitive to the selected transects and the outcomes are not affected if individual sections are used as opposed to a mean. The distribution of the averaged SR1b section occupations through the time series might result in the aliasing of any long-term trends in the early to late summer means. However, as discussed by *Meredith et al*. [2011], there is no clear long-term trend in water mass properties along Drake Passage. The seasonal change in water mass area within Θ-S space for CARS is determined in the same way; however, the early summer water mass area distribution uses the climatological estimate for November, whereas the late summer uses both the February and March estimates.

2.3. Calculation of Dia-Surface Transformations Inferred From Air/Sea Fluxes

The transformation of sea-surface Θ-S classes can be determined from air/sea fluxes of heat and freshwater. *Speer* [1993] presents a method to calculate the transformation implied by surface air/sea fluxes in thermohaline coordinates. Dia-thermal (F_Θ) and dia-haline (F_S) transformations are determined by calculating the amount of water converted by the integrated heat and freshwater flux over the area (A) within each sea-surface Θ and S class:

$$F_\Theta(\Theta,S)=\int\frac{\Pi(\Theta,\Theta^*)}{\Delta\Theta}\Pi(S,S^*)\frac{Q_{net}}{\rho C_p}dA;\tag{10}$$

$$F_S(\Theta,S)=\int\Pi(\Theta,\Theta^*)\frac{\Pi(S,S^*)}{\Delta S}f_{net}S dA.\tag{11}$$

Again Π is a boxcar function that is either 0 when Θ or S is outside the range defined by the given Θ-S class, or 1 when Θ and S are within this range. Q_{net} and f_{net} are the net surface heat flux (W m^{-2}) and E − P (m s^{-1}),

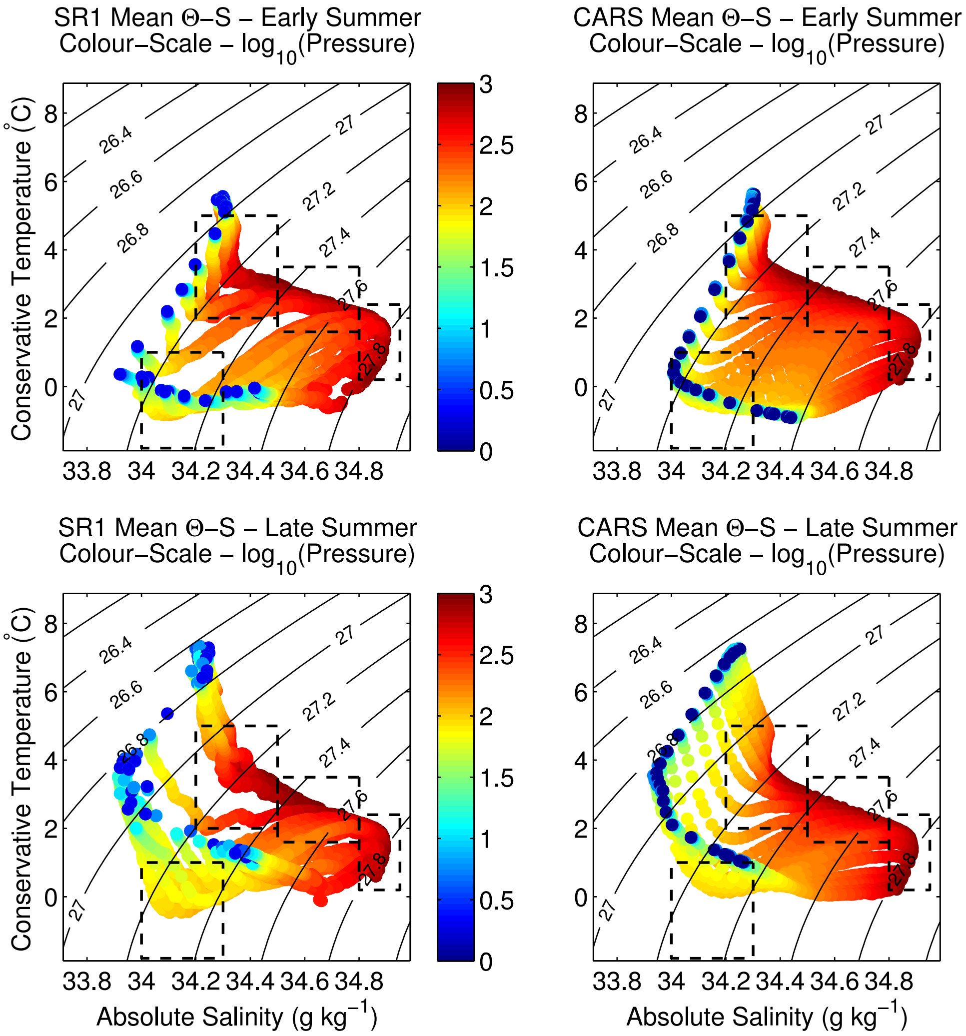

Figure 3. (top row) Mean early summer and (bottom row) late summer Θ-*S* profiles from the (left column) SR1b section occupations and the (right column) CARS seasonal climatology. The color scale indicates the $\log_{10}$ pressure of each observation. The dashed boxes show the locations of (from left to right) AAWW, AAIW, UCDW, and LCDW.

respectively, ρ is the density and C_p is the specific heat capacity of seawater. Here $\int dA$ represents an integral over an area of the sea-surface occupied by a given Θ-*S* class. This calculation of F_Θ differs from that used by *Speer* [1993] through the use of density, converting the mass flux calculated by *Speer* [1993] to a volume flux. Thus, F_Θ and F_S are in units of $\text{m}^3\ \text{s}^{-1}$. When calculating these fluxes over a two-dimensional ocean transect as done here, dA becomes dL, where L is the length-scale defined by each sea-surface Θ-*S* class, giving a flux in units of $\text{m}^2\ \text{s}^{-1}$.

From the dia-surface transformations calculated using equations (10) and (11), the inferred volume change can be computed using equation (6) by populating **x** with F_Θ and F_S, giving **b**, the rate of change of volume due to air-sea fluxes, which when multiplied by the relevant time-interval yields the volume change. This surface buoyancy flux-inferred volume change can then be removed from the observed volume change, giving a residual volume change. Residual dia-surface transformations can then be calculated by populating **b** with the residual volume change divided by the time interval, and solving for **x** as in section 2.2 for the total dia-surface transformations. From equation (1), this gives the residual dia-surface transformations due to diffusive processes if an entire Θ-*S* volume is enclosed. If the entire volume is not enclosed, so that all the water of a given Θ-*S* class is not captured within the geographical domain used, transport of this particular class across the geographical boundary will imprint as a dia-surface transformation. Similarly, for a two-dimensional transect where water mass area is considered, as opposed to water mass volume, this residual will also include a component associated with changes in the advective transport of water through the boundaries of the geographical domain used. In both cases, these volume transports would manifest in the term ϵ in equation (5).

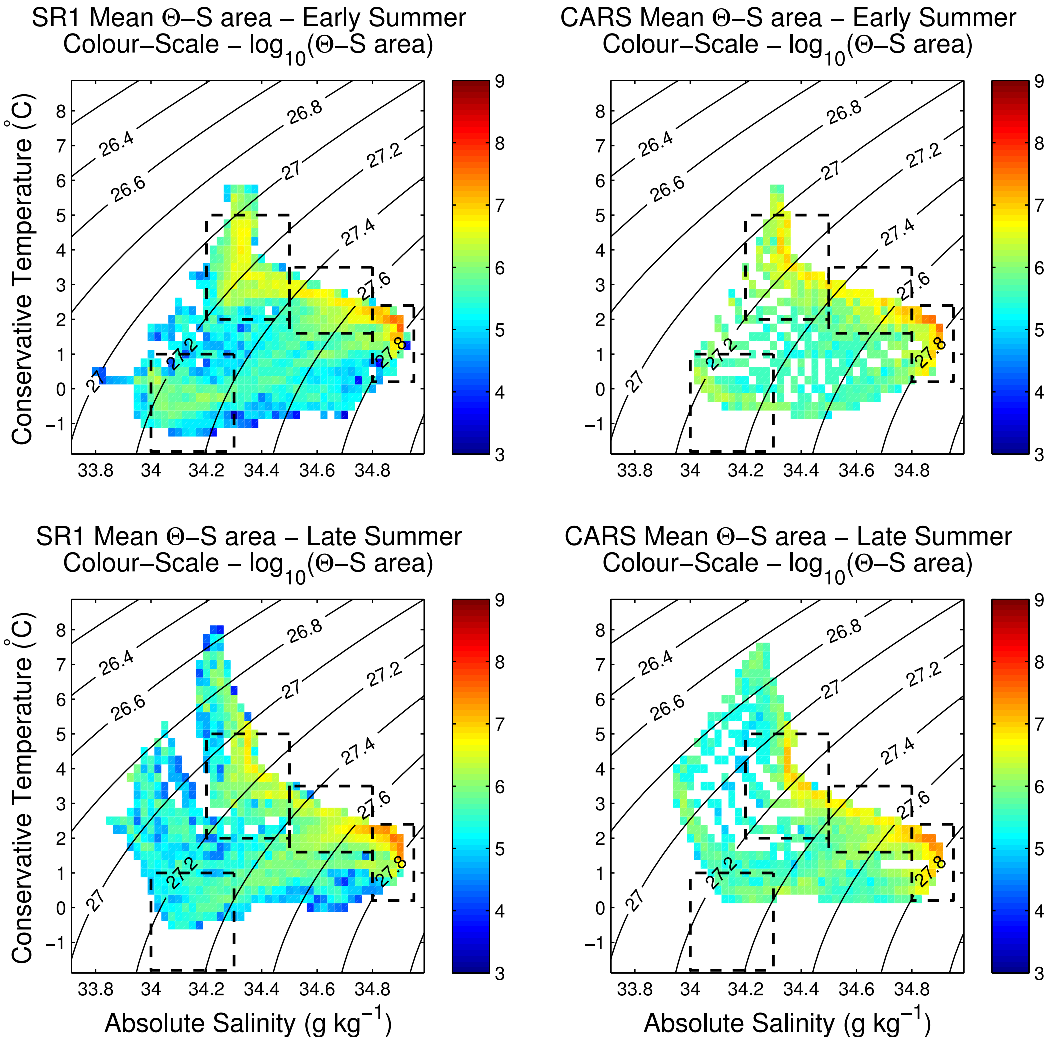

Figure 4. (top row) Mean early summer and (bottom row) late summer Θ-*S* area from the (left column) SR1b section occupations and the (right column) CARS seasonal climatology. The color scale indicates the $\log_{10}$ area of each Θ-*S* class. The dashed boxes show the locations of (from left to right) AAWW, AAIW, UCDW, and LCDW.

3. Drake Passage From an Eulerian Perspective

To provide a comparative framework in which to present the water mass changes within Drake Passage in thermohaline coordinates, we first discuss early to late summer changes from an Eulerian perspective, i.e., in latitude-pressure coordinates. In Eulerian coordinates, a mean of the SR1b section occupations in November is used to represent early summer. This is compared with a mean late summer transect determined using the three section occupations from February 2000, February 2009, and March 2013 (left column, Figure 1). These are compared with mean transects taken from the CARS climatology using the same combination of months (right column, Figure 1).

In the early summer along SR1b mean, surface and near-surface waters are generally cooler, in particular a thick tongue of cold ($\Theta < 0°$C) and fresh ($S < 34.2$g kg^{-1}) AAWW extends northward from the Antarctic continent (Figure 1, first four plots). This layer is less pronounced later in the summer, while surface waters are in general warmer and fresher. Underlying these seasonal surface water masses is a wedge of relatively salty CDW with $S < 34.8$g kg^{-1}. Discerning any change in the properties of these deeper water masses is difficult given the large variability in the depth of isopycnals surrounding them. This is likely the result of aliased mesoscale variability, also evidenced by the lenses of ~2°C water that have been advected across the Polar-Front (PF) and are evident in both early and late summer.

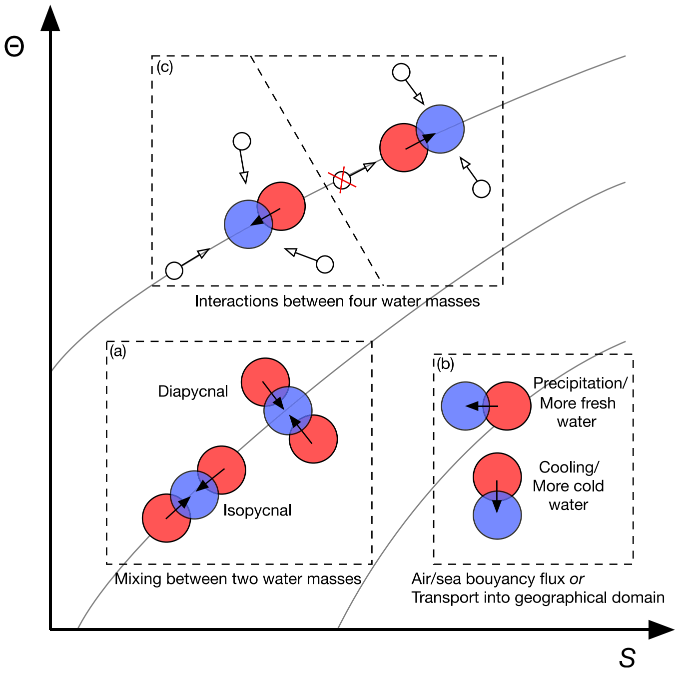

Figure 5. A simplified representation of the processes that can change the location of water mass area within Θ-*S* space. In each a red circle represents the initial location of a water mass in Θ-*S* space, and a blue circle represents the final location. The black arrows are the dia-surface transformations of water mass area associated with the redistribution. In the case of box (c), which describes the interactions of four water masses, the unfilled arrows represent the direction from which each water mass (unfilled circles) is mixing. This relates to the process affecting the location of AAIW within Θ-*S* space during (left) winter and (right) summer and its relation to the presence of AAWW (e.g., bottom left unfilled circle) as discussed in section 7.

The CARS climatology generally replicates the mean properties represented by the SR1b section observations, differing only in the absence of the mesoscale related variability (Figure 1, first four plots, right column). Further, the wedge of CDW appears to be less extensive in the climatology and shows very little change during the summer.

The change in Θ and *S* from early to late summer (Figure 1, bottom four plots) highlights some of the difficulties in determining change within an Eulerian coordinate system. The change according to the SR1b section data gives a generally coherent warming (>2°C) and freshening (<-0.015 g kg^{-1}) at the surface where the seasonal change is large (Figure 1, left column, bottom two plots). Below the surface the pattern of change is much less clear due mostly to aliased mesoscale variability, with an apparent cooling of up to 2°C and an increase in *S* as high as 0.2 g kg^{-1} in the region of the PF. In the absence of these mesoscale fluctuations, the CARS climatology again shows a coherent warming and freshening in the surface with similar magnitude, but suggests a more coherent area of weaker cooling and salinification below the surface, coinciding roughly in location with the largest subsurface changes according to the SR1b section data. The proximity of these changes to the PF makes disentangling the relative contribution of diabatic and adiabatic changes difficult given the impact of frontal migration in this region.

4. Drake Passage in Thermohaline Coordinates

In this section, we discuss changes in water mass properties in thermohaline coordinates within Drake Passage, comparing data from the SR1b section occupations and the CARS climatology. These results are then interpreted in section 7. To provide some geographical context to the Θ-*S* observations, the mean Θ-*S* profiles from the SR1b transects used in section 3 are plotted in Figure 3, where the color scale represents the pressure associated with each measurement. In both the observations and the CARS climatology, the UCDW and the saltier LCDW make up the shoulder of measurements characterized by the pycnocline that shoals from the northern to the southern end of the transect, and is mostly set by a strong gradient in *S* between the fresher SAMW/surface waters and the saltier UCDW and LCDW. According to the SR1b section, occupations (and to some extent the climatology) surface and near-surface observations (blues to yellows) are grouped into two regions of Θ-*S* space, which are geographically separated by the PF. This separation is exaggerated by the late summer as the *S*-minimum associated with AAIW at 4°C and 34.3 g kg^{-1} is reduced. From early to late summer, the surface waters in general become warmer and fresher in both data sets. The subsurface AAWW is apparent in both the climatology and the observations, but is approximately 0.2°C warmer in the climatology. The AAWW warms from early to late summer in both data sets.

The distribution of water mass area within thermohaline coordinates and the early to late summer change in distribution (determined as described in section 2.2) is similar according to the SR1b section occupations and the CARS climatology (Figure 4, left and right plots, respectively). The region of largest water mass area

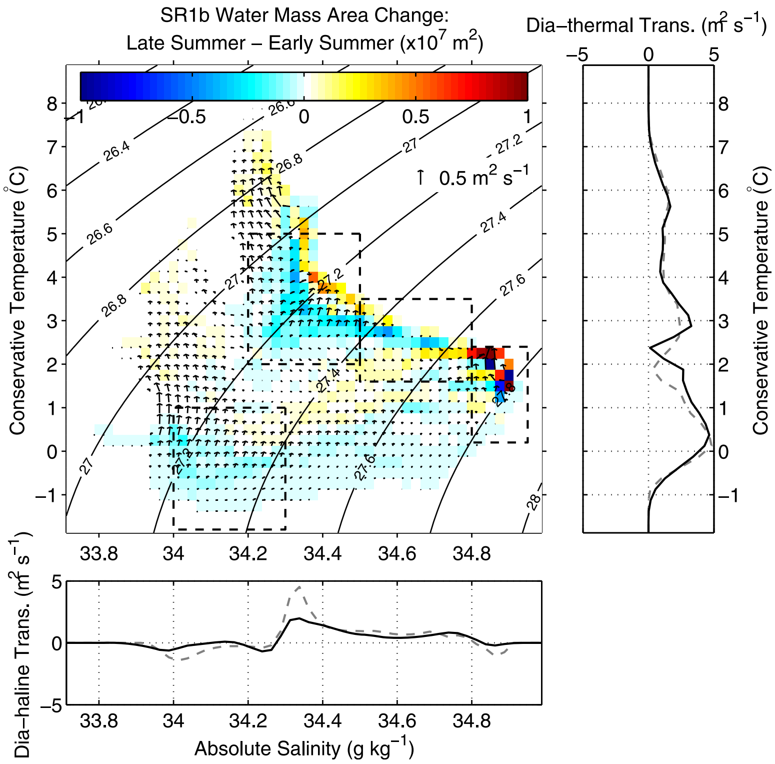

Figure 6. Θ-*S* area change (color scale) and associated dia-surface transformations (arrows) from early summer to late summer from the SR1b section occupations. The right and bottom plots are the summed dia-thermal and dia-haline transformations, respectively (black lines: SR1b section occupations, gray lines: CARS climatology). Area change has units of 1×10^7 m^2. Transformations have units of m^2 s^{-1}. The dashed boxes show the locations of (from left to right) AAWW, AAIW, UCDW, and LCDW.

is associated with LCDW ($\Theta \sim 2°$C and $S \sim 34.9$ g kg^{-1}). Both data sets resolve a ridge of high water mass area either side of the PF, the warmer side of which is made up of UCDW and AAIW. The peak at the coldest and freshest extent of the ridge associated with the region south of the PF highlights the seasonally formed AAWW. The erosion of AAWW from early to late summer is evident both as a decrease in water mass area at this region of Θ-*S* space and as a redistribution of water mass area into warmer and fresher regions of Θ-*S* space. Also evident is a redistribution of surface water masses to a warmer and fresher region of Θ-*S* space.

The information in Figures 3 and 4 enables a clear description of the early to late summer changes in water mass properties within Drake Passage. These seasonal changes described in thermohaline coordinates are not aliased by frontal migration or the adiabatic processes associated with mesoscale variability apparent in the left plot of Figure 1. Furthermore, they provide an initial basis for a quantitative assessment of the balance between the diabatic exchanges of buoyancy that drive the observed seasonal changes. We will now discuss the associated dia-surface transformations derived from the change in water mass area between early summer and late summer.

For an entirely enclosed water mass *volume*, the change in the distribution of this volume within Θ-*S* space and the derived dia-surface transformations will be entirely diabatic. A change associated with surface buoyancy forcing will therefore appear as a redistribution to a different region in Θ-*S* space according to the applied buoyancy flux (e.g., Figure 5b). In contrast, both isopycnal and diapycnal mixing of two water masses in different regions of Θ-*S* space will appear as dia-surface transformations that converge to the mean Θ and *S* of the two water masses that are being mixed (e.g., Figure 5a). In this investigation, where we are analyzing the seasonal change within a two-dimensional ocean transect and discussing this change in terms of water mass *area*, the case that all changes are diabatic is not true. The analysis of an ocean transect using this method, as with other methods, is subject to the adiabatic change associated with variability in the meridional and zonal advection of water in geographical coordinates through the geographical boundary of the domain from which water mass area is determined (ϵ term, RHS equation (5)). In this case, an adiabatic change will appear as a redistribution of water mass area to a different region in Θ-*S* space, with a similar appearance to a diabatic change driven by surface buoyancy fluxes (Figure 5b). For example,

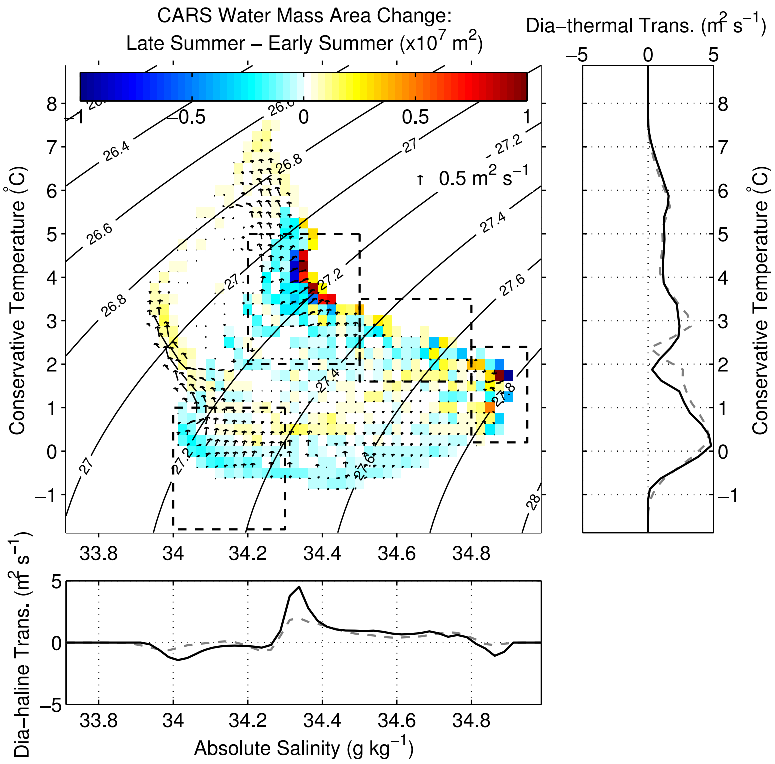

Figure 7. Θ-*S* area change (color scale) and associated dia-surface transformations (arrows) from early summer to late summer from the CARS climatology. The right and bottom plots are the summed dia-thermal and dia-haline transformations, respectively (black lines: CARS climatology, gray lines: SR1b section occupations). Area change has units of 1×10^7 m^2. Transformations have units of m^2 s^{-1}. The dashed boxes show the locations of (from left to right) AAWW, AAIW, UCDW, and LCDW.

an increase in the amount of cold salty water transported into the section geographically, would imprint as negative dia-thermal and positive dia-haline transformations in Θ-*S* space. The advantage of this method is that it should be clearer, with some interpretation, where these advective processes are affecting the distribution of water mass area within Θ-*S* space, based on a comparison with the implied dia-surface transformations derived using the seasonal surface air/sea fluxes and the estimated area change due to ϵ.

The early to late summer change in water mass area and the associated dia-surface transformations are characterized by a redistribution of water to a generally warmer region within Θ-*S* space (Figures 6 and 7, SR1b and CARS, respectively). The area changes for both the SR1b section occupations and the CARS climatology indicate a warming of the ridges of high water mass area highlighted in Figure 4. The largest changes occur in the AAIW (~4°C and 34.4 g kg^{-1}). Large changes in water mass area also occur in the UCDW and the LCDW. The loss of water mass area from the coldest and freshest region within Θ-*S* space reflects the seasonal erosion of AAWW over the summer. The transformation vectors in Figures 6 and 7 show the minimum transformation required to produce the observed change in water mass area. These transformations may not reflect the actual path within Θ-*S* space taken by each parcel of water; however, given the temporal resolution of both data sets, the black arrows represent as much as can be inferred regarding the direction and magnitude of the transformations.

In the surface and near-surface waters of the section occupations and the climatology, that is near the region of lowest *S* along the ridges of high water mass area, the direction of the dia-surface transformations reflects a warming and freshening. These transformations have magnitudes of the order of 0.5 m^2 s^{-1} and are typically diapycnal in direction. The erosion of AAWW seems to be driven by a mostly dia-thermal transformation with a minimal dia-haline component. This is consistent in both data sets. The dia-surface transformations in the deeper water masses are larger when determined using the section occupations. They have magnitudes of <0.3 m^2 s^{-1} with a warming and salinification in the AAIW, a consistent positive dia-haline component throughout the UCDW, but a warming at $\Theta < 1$°C and a cooling at $\Theta > 1$°C. For the LCDW in the region of highest *S*, dia-surface transformations have a positive dia-thermal component, with negative and positive dia-haline components converging at 34.85 g kg^{-1}. The dia-surface transformations in the deeper water masses

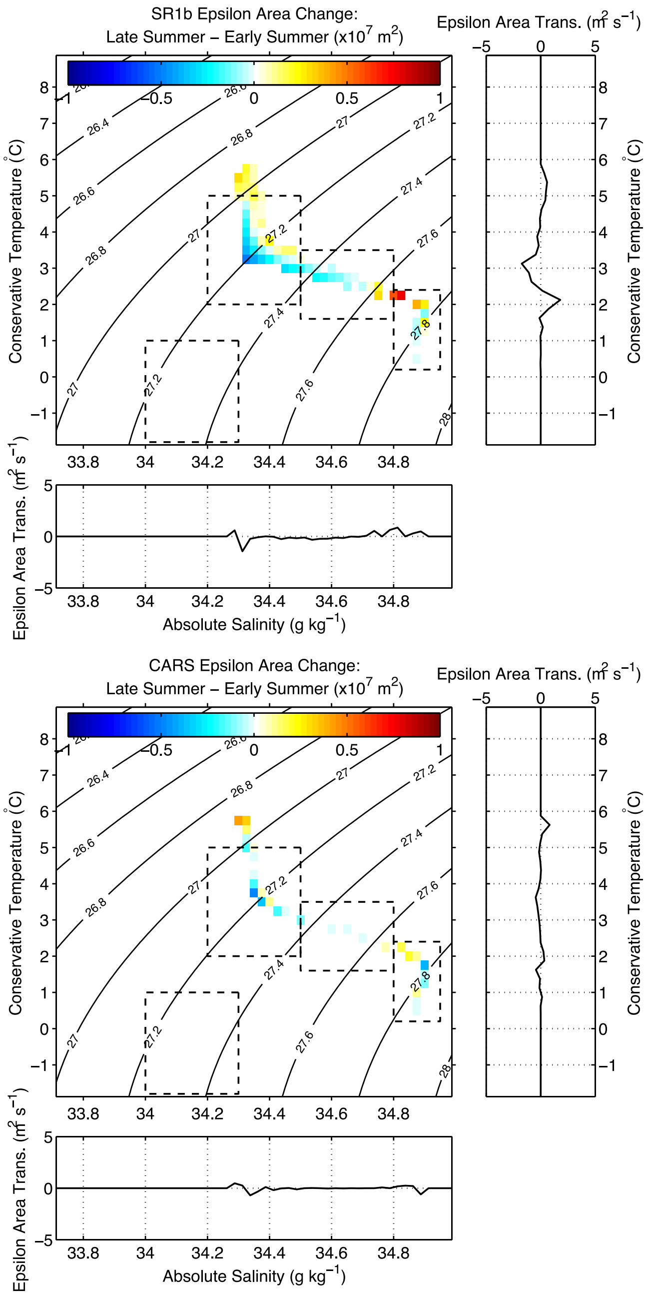

Figure 8. Θ-S area change associated with the ϵ term in equation (5) for the (top) SR1b section occupations and the (bottom) CARS seasonal climatology. Area change has units of 1×10^7 m^2. Solid lines in the bottom and right plots indicate the Θ-S area change summed across all Θ or S divided by the time-interval from early to late summer (3.5 months) to compare to Figures 6 and 7. The dashed boxes show the locations of (from left to right) AAWW, AAIW, UCDW, and LCDW.

are much weaker according to the seasonal climatology. The transformations have a similar direction, but differ with a convergence of vectors in the LCDW at a Θ and S of $\sim$1°C and 34.8 g kg^{-1}.

The dia-haline and dia-thermal transformations summed across all values of Θ and S, respectively, for both the section occupations (Figure 6, bottom/right plot) and the seasonal climatology (Figure 7, bottom/right plot) are similar. Exceptions are a negative dia-thermal transformation that is evident only in the section occupations between 2 and 3°C and a negative dia-haline transformation at $S > 34.8$gkg^{-1} in the seasonal climatology. These differences between the section occupations and the climatology are likely an aliasing of a change in either the zonal or meridional advection of water through the section that is aliased to a greater extent by the averaging of the section occupations.

Solving for ϵ in equation (5) provides an estimate of the transport through the geographical boundary of the section. The volume change associated with ϵ for both the SR1b section occupations (Figure 8, top) and the CARS climatology (Figure 8, bottom) indicate an increase of water mass area in the LCDW, suggesting a flow of LCDW into the geographical domain of the section. There is also a loss of water mass area in the AAIW, suggesting a flow of AAIW out of the geographical domain of the section. The degree to which the changes of water mass area associated with ϵ calculated in this way reflect the actual transport into and out of the geographical domain of the section remains unclear. However, this approach could be tested using a numerical model where the volume transports can be easily determined.

We next describe the early to later summer dia-surface transformation and resultant area change inferred from the sea-surface fluxes of heat and freshwater from the WHOI climatology. The following analysis was also performed using the NOCSv2 climatology. This comparison is discussed in Appendix A, which shows that there is no substantial difference between the inferred transformations discussed below. To determine

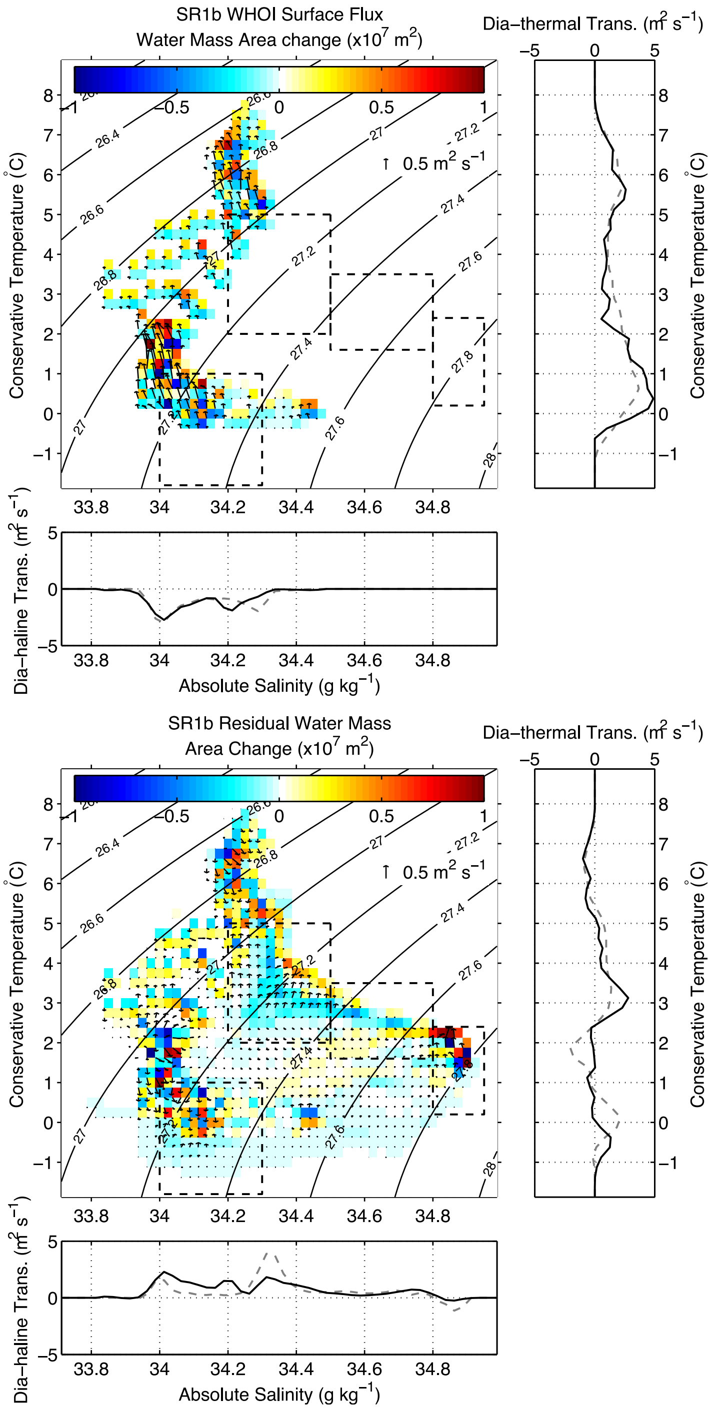

Figure 9. (top plots) As in Figure 6 but showing dia-surface transformations and Θ-*S* area change inferred from the WHOI surface flux climatology, and (bottom plots) the resultant residual dia-surface transformations and Θ-*S* area change from the SR1b section occupations. The surface flux area change and associated dia-surface transformations are determined cumulatively from the surface heat and freshwater fluxes between early and late summer. The residual area change and associated dia-surface transformations are calculated by subtracting the sea-surface flux-inferred area change from the total area change (color scale in Figure 6). Area change has units of 1 × 10^7 m^2.

a smooth seasonal transition from early to late summer, the surface fluxes and the sea-surface Θ and *S* were linearly interpolated to a high temporal resolution of approximately 6 days. The dia-surface transformations were determined for each time step, and the sum of the resultant area change was calculated for all the resultant time steps. This sum was then used to determine the total implied dia-surface transformation, which is shown in Figures 9 and 10. If this interpolation is not performed then the inferred area change is restricted to a small region of Θ-*S* space, and does not mimic the broad redistribution apparent at the surface in Figures 6 and 7. An interpolation with a lower temporal resolution results in data-less regions of Θ-*S* space.

The implied water mass area change and dia-surface transformations indicate ubiquitous warming and freshening of all surface water masses from early to late summer (Figures 9 and 10, SR1b/CARS, respectively), with transformations up to 0.5 m^2 s^{-1} in the regions of Θ-*S* space with high water mass area separated geographically by the PF. This separation is evident as peaks in the plots of the dia-thermal and dia-haline transformations in the top plots of Figures 9 and 10, summed across all *S* and Θ, respectively. The pattern of water mass area change shown in Figures 9 and 10 is noisy and patchy. This partly reflects the noise within the air-sea flux data, but also the impact of strong gradients in Θ and *S* across the PF.

The area change, determined from air/sea fluxes can be subtracted from the total area change shown in Figures 6 and 7 to give a residual area change, and therefore transformation. The resultant pattern of area change and the vectors of transformation remain unchanged from the net change shown in Figures 6 and 7 for the majority of Θ-*S* space away from the sea-surface (Figures 9 and 10, bottom plot). The net water mass area change and transformation in the surface water masses (e.g., Figures 6 and 7) are smaller than the transformation and change inferred from the air/sea fluxes. The result is a residual negative dia-thermal transformation and positive dia-haline transformation for those surface water masses that are parallel to the slope of the Θ-*S* profiles, suggesting a downward mixing of the seasonally warmed and freshened surface water with the generally cooler and saltier subsurface water. The convergence of vectors to ~0°C and 34.1 g kg^{-1} within Θ-*S* space (bottom plots of Figures 9 and 10) indicates the erosion of the AAWW during the summer. The direction of the vectors suggests this process is underpinned by diapycnal mixing (see Figure 5a).

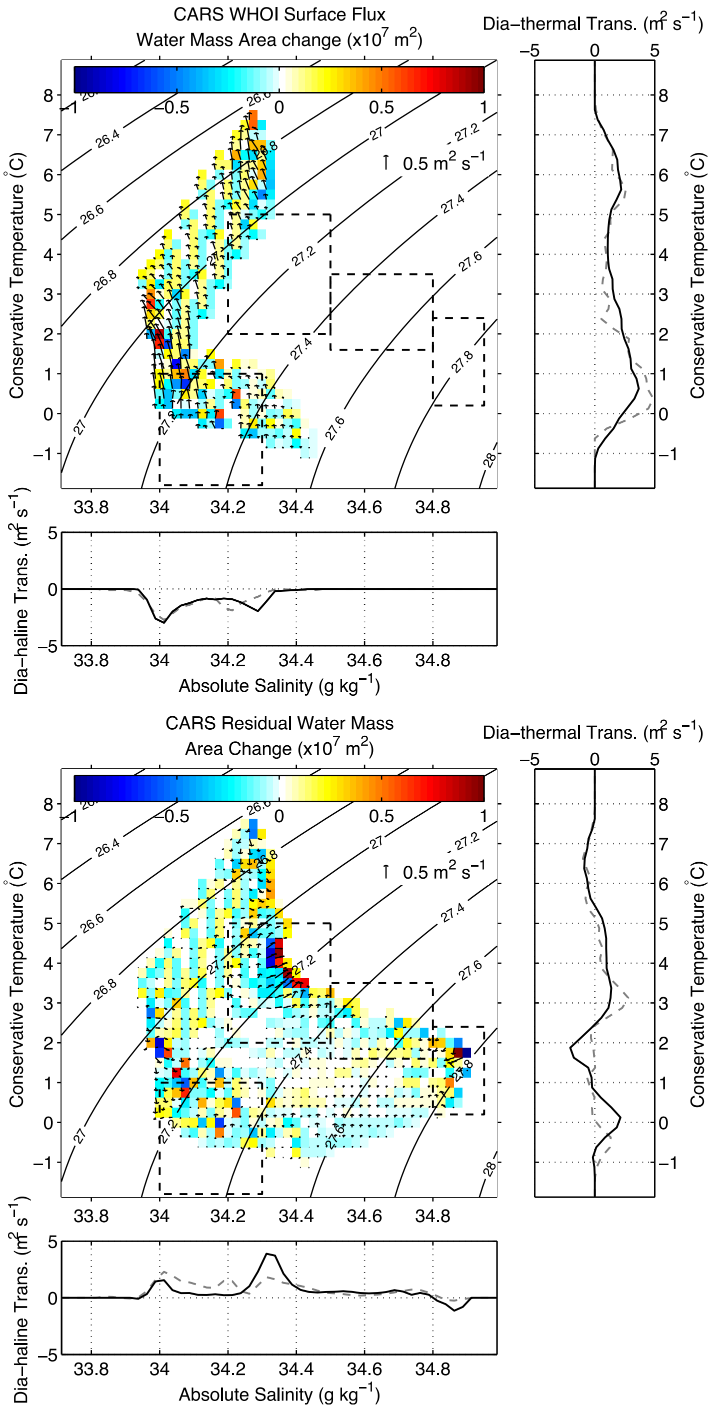

Figure 10. (top plots) As in Figure 7 but showing dia-surface transformations and Θ-*S* area change inferred from the WHOI surface flux climatology, and (bottom plots) the resultant residual dia-surface transformations and Θ-*S* area change from the CARS climatology. The surface flux area change and associated dia-surface transformations are determined cumulatively from the surface heat and freshwater fluxes between early and late summer. The residual area change and associated dia-surface transformations are calculated by subtracting the sea-surface flux-inferred area change from the total area change (color scale in Figure 7). Area change has units of 1 × 10^7 m^2.

5. Austral Winter Thermohaline Water Mass Changes Along Drake Passage in a Seasonal Climatology

The early to late summer changes along Drake Passage within thermohaline coordinates according to the SR1b section occupations and the CARS seasonal climatology agree well, providing confidence in the use of both data sets especially given the sparse temporal nature of the SR1b section occupations and the impact of mesoscale variability in this data set. We will now discuss the entire seasonal cycle more fully by analyzing the winter water mass area changes along Drake Passage using the CARS

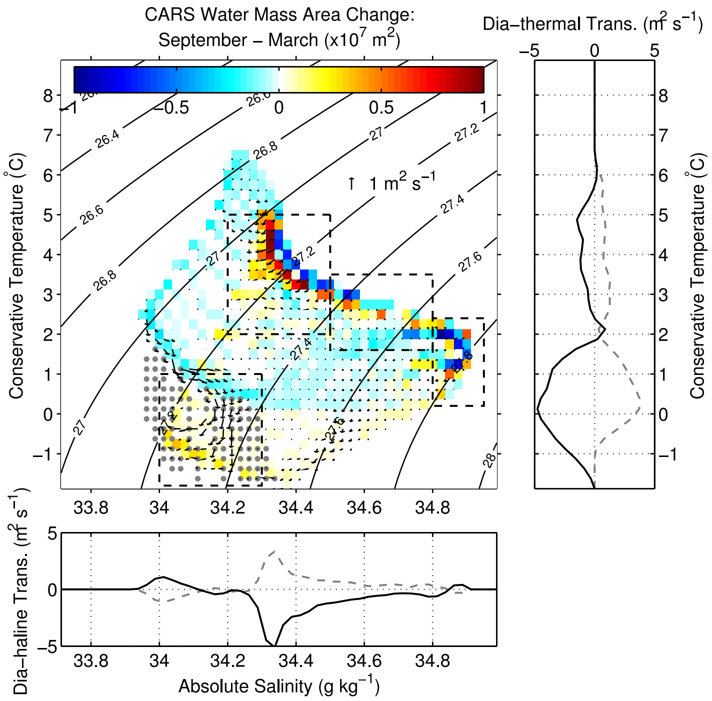

Figure 11. Seasonal winter (March–September) change of Θ-*S* area change and associated dia-surface transformations from the CARS seasonal climatology (right column). The right and bottom plots are the summed dia-thermal and dia-haline transformations, respectively (black lines: winter fluxes, gray lines: summer fluxes). Gray stippling indicates Θ-*S* classes in which air/sea flux data were unavailable at some point between March and September. Area change has units of 1×10^7 m^2. Transformations have units of m^2 s^{-1}. The dashed boxes show the locations of (from left to right) AAWW, AAIW, UCDW, and LCDW.

climatology over the winter period from March to September. It is important to note that there is no air/sea flux data available in the southernmost region of the SR1b section, so that important information regarding the processes affecting AAWW formation is absent from the coldest regions of Θ-*S* space in Figures 11 and 12 as highlighted by the gray stippling in these figures. The total water mass area change and the associated dia-surface transformation (Figure 11) in general indicate a pattern of water mass area redistribution that opposes the change from early to late summer (e.g., Figure 7). At the surface (fresher region in Θ-*S* space), there is a cooling and salinification. In the AAIW, there is a general freshening cooling, and a warming and freshening in the UCDW. There is a slight divergence of vectors in the LCDW, with an increase of water mass area in the region of highest *S*, and at $\Theta < 1°$C there is a cooling.

The dia-surface transformations inferred from air/sea fluxes (Figure 12, top plot) maintain a negative dia-haline component throughout the winter season so that buoyancy loss is driven by a strong negative dia-thermal transformation. The freshening implied by the surface air/sea fluxes highlights the importance of mixing in driving the positive dia-haline transformation in surface waters (low *S*, Figure 11). This process can be seen in Figure 12 (bottom plot) as a convergence of vectors at $S \sim 34.3$ g kg^{-1} and $\Theta \sim 4°$C. Thus, the general seasonal change in water mass area during winter, in regions unaffected by sea-ice, is driven by a balance between the sign of the surface buoyancy inferred dia-thermal transformation and the residual dia-surface transformation controlled by the interaction through mixing of the surface water masses and the colder and saltier deep water.

6. Projection of Thermohaline Changes into Eulerian Coordinates

A projection into a fixed geographical Eulerian coordinate system of the water mass changes and the implied dia-surface transformations calculated within thermohaline coordinates provides a visualization that is directly comparable to the changes shown in the bottom two plots of Figure 1. This was done by finding the observations in Eulerian coordinates of Θ and *S* that match each class in thermohaline coordinates, and assigning the dia-thermal and dia-haline components of the area weighted transformations to the corresponding latitude and pressure. These values were converted to a Θ or *S* change through multiplication with the grid spacing of Θ or *S* in thermohaline coordinates, respectively, and the time difference from early to later summer, which was 3.5 months. To reduce noise caused by the loss of information resulting from the initial projection into Θ-*S* space, this reprojection was performed individually with each SR1b section used for the calculation of water mass area change and the resultant Θ or *S* change was averaged. Such loss of information is associated with the process of averaging in Θ-*S* space, which removes some of

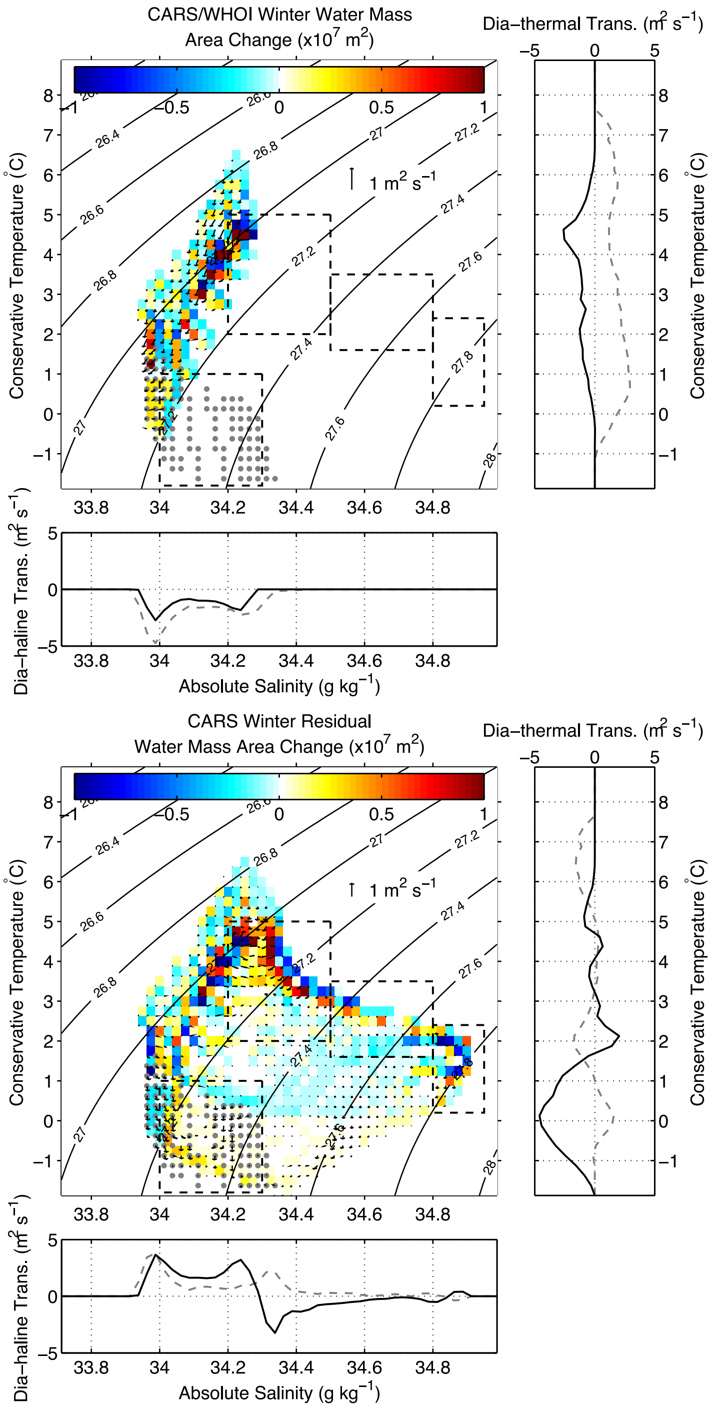

Figure 12. (top) As in Figure 11 but showing the seasonal winter change of water mass area and associated dia-surface transformations inferred using the WHOI surface flux climatology, and (bottom) the seasonal winter change of the residual water mass area and associated dia-surface transformations calculated by removing the water mass area change due to air/sea fluxes (top plot) from the total winter change shown in Figure 11. Again the arrows represent the associated dia-surface transformations inferred from the residual area change. Area change has units of 1 × 10^7 m^2.

variability associated with the positions of each water mass in geographical coordinates. For the CARS climatology, the reprojection was performed for each month from November to February and the resultant Θ or *S* change was then averaged for this period.

A comparison between the reprojected changes of Θ and *S* in latitude/pressure coordinates in both data sets is promising (Figures 13 and 14/15 and 16, SR1b/CARS, respectively), the exception being the southernmost region of the SR1b section occupation reprojection which have strong increases in both Θ and *S* that could be the result of particularly cold water masses which warm strongly according to our analysis but are only observed a small number of times. As these waters do not exist at all in CARS, this intense warming is not seen. The SR1b section data show changes in Θ and *S* down to 3000 m and use the dia-surface transformations derived from the full ocean depth section occupations. Of particular interest is a freshening and slight warming of the saltier LCDW, an opposing cooling and increase in *S* in the deeper variety of the UCDW, a slight warming and salinification of the shallower UCDW and AAIW, and a warming of the deep waters near the Antarctic continent. A comparison between the reprojected changes in Θ and *S*, and the changes shown in the bottom rows of Figure 1 suggest a better agreement with the CARS change. That the reprojected changes in Θ and *S* from the SR1b section occupations are similar to both the realizations of changes in Θ and *S* from the CARS climatology suggest that this method has successfully removed the aliased adiabatic mesoscale variability that originally dominated the changes shown in Figure 1.

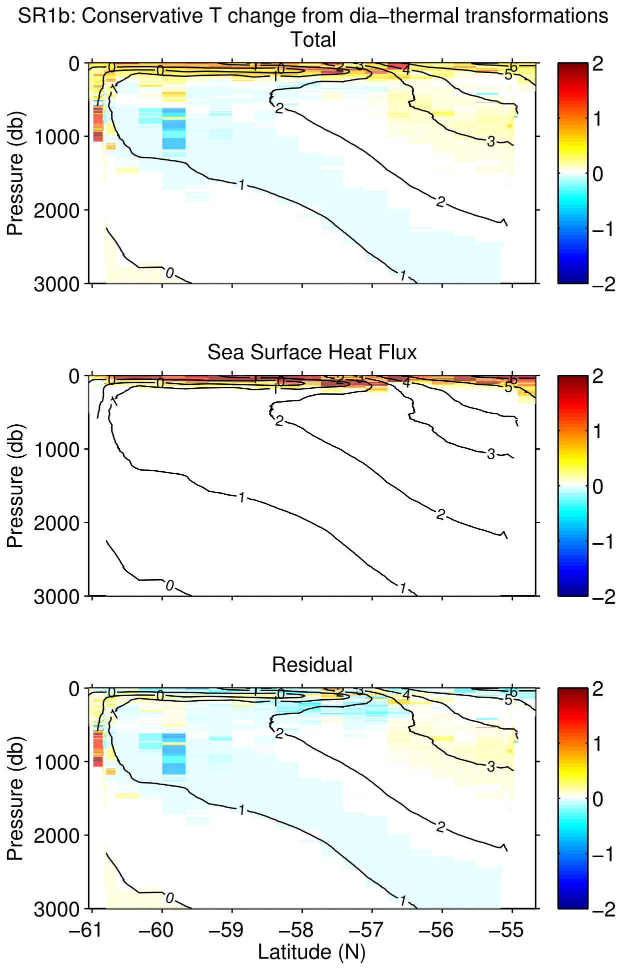

Figure 13. (top) The implied early to late summer change in Θ calculated from the total, (middle) surface buoyancy inferred, and (bottom) residual fluxes of water mass area calculated using the SR1b section occupations down to 3000 m and the WHOI air/sea flux product. Black contour lines indicate mean Θ. Units °C.

7. Discussion and Interpretation

The general picture of the Southern Ocean overturning is well established, where the prevailing westerly wind drives upwelling of LCDW and UCDW which are transformed by air-sea-ice buoyancy exchange and mixing [*Rintoul and Naveira-Garabato*, 2013]. Depending on the sign of these buoyancy fluxes, these deep water masses are either made denser and sink as AABW close to the Antarctic continent, or are made more buoyant and are eventually subducted equatorward of the PF as either AAIW or SAMW [*Speer et al.*, 2000; *Talley*, 2013]. The impact of seasonality on the water masses of the Southern Ocean is less well known as a result of a poor understanding of air-sea-ice buoyancy fluxes during the austral winter due to a lack of observations [*Schulz et al.*, 2012]. For example, the presence of cold/fresh AAWW and its seasonal cycle of formation/destruction as the remnant of the winter mixed layer is accepted [*Park et al.*, 1998], but the role of AAWW in establishing the characteristic salinity minimum of AAIW is controversial [*Naveira Garabato et al.*, 2009]. *Naveira Garabato et al.* [2009] attribute the formation of AAIW to the year-round frontal mesoscale subduction of AAWW and relate interannual changes in properties of AAIW within Drake Passage to the properties of AAWW as set during the winter by the major modes of Southern Hemisphere climate variability. This is contradictory to the notion that AAIW is formed during the winter at specific locations in the South Pacific and South Atlantic [*Talley*, 1996].

From the analysis of seasonal thermohaline water mass area distribution along Drake Passage, we propose that it is possible to resolve the upwelling (CDW) and downwelling (AAIW/SAMW) limbs of the Southern Ocean overturning within Drake Passage that are enabled by the seasonal changes of buoyancy exchanged between the atmosphere and ocean. Note that although upwelling and downwelling may be driven by Ekman pumping, the transformation from one water mass to another requires surface buoyancy fluxes. The formation and gradual subduction of AAIW is evidenced in the region of Θ-*S* space centered at $S \sim 34.3\ \mathrm{g\ kg^{-1}}$ and $\Theta \sim 4°\mathrm{C}$ in Figures 3–12 from both the section occupations and the seasonal climatology. First, in this region of Θ-*S* space, the early summer Θ-*S* profiles in Figure 3 (top row) show the distinct *S*-minimum characteristic of AAIW. By late summer (bottom row, Figure 3), this *S*-minimum is less clear. This process is similarly manifest in the change of water mass area from early to late summer in both data sets as an apparent isopycnal redistribution of water mass area to a warmer and saltier region of Θ-*S* space, emphasized by a positive dia-thermal and dia-haline transformation. AAWW is eroded during the summer, becoming warmer through diapycnal mixing from above emphasized by the convergence of positive and

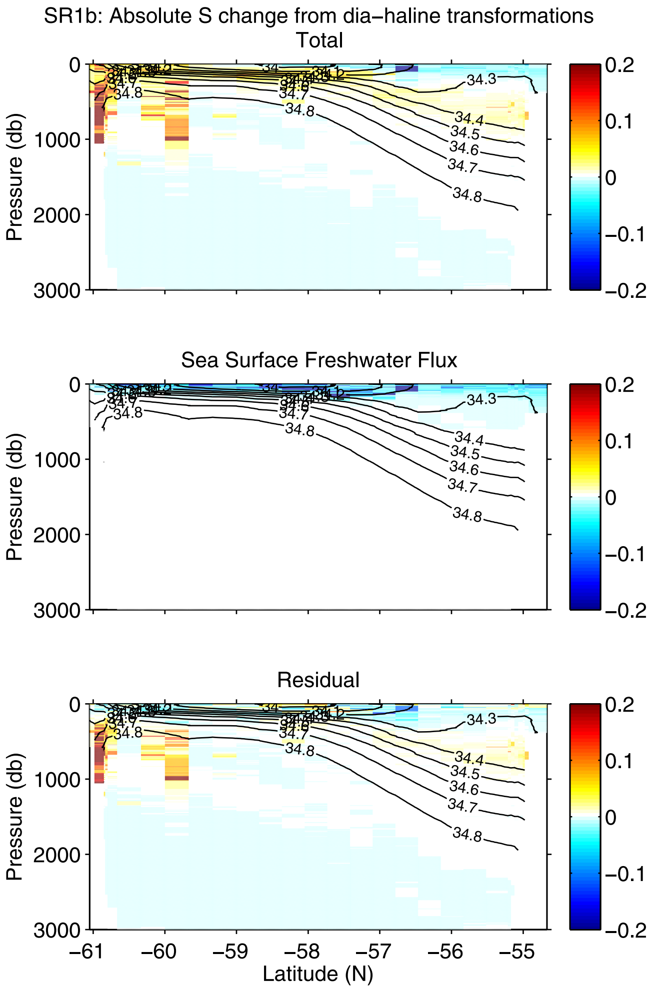

Figure 14. As in Figure 13 but showing the implied seasonal change in *S*. Black contour lines indicate mean *S*. Unit: g kg^{-1}.

negative residual dia-thermal transformations. Regarding upwelling and transformation of CDW, the UCDW between 34.4 and 34.8 g kg^{-1} and at $\Theta > 1°C$ is in general getting saltier, the warmest variety is getting warmer, and the coldest variety of UCDW is getting colder (see Figures 13–16). Finally, the salty LCDW ($S > 34.8$g kg^{-1}) gets slightly warmer and fresher during the summer.

In comparison, during winter (Figures 11 and 12) we see a gain in water mass area in the region of Θ-*S* space associated with the *S*-minimum of AAIW, with negative dia-thermal and dia-haline transformations and an isopycnal redistribution of water mass area. Further, by the end of winter the *S*-minimum is reestablished, signifying the presence of a colder and fresher variety of AAIW. AAWW formation is extensive but we have no knowledge of the actual air-sea-ice buoyancy exchange that drives AAWW formation. We do see a residual salinification and cooling of surface water north of the PF despite consistently negative E − P fluxes. A positive dia-thermal and negative dia-haline transformation in the UCDW highlight a warming and freshening during the winter, in comparison to a slight cooling and salinification of the LCDW.

The following interpretation is also represented schematically in Figure 17. These observations suggest that AAIW is gradually subducted and transformed during the summer and formed in excess during the winter. In winter, the *S*-minimum of AAIW is established as UCDW (which gets fresher), surface waters (which get cooler and saltier), and AAWW (as it is formed during the winter) mix. The warming and salinification of AAIW during the summer emphasizes the importance of cold and fresh AAWW in maintaining the *S*-minimum of AAIW, suggesting the interaction of these water masses is reduced during the course of the summer as AAWW is eroded and made less dense once capped. If mixing between the surface water, AAIW and UCDW continued during the summer (with a reduced cold/fresh source of AAWW), the resultant redistribution of water mass area would reflect the isopycnal shift we observe in Θ-*S* space, represented schematically in Figure 5c. Further, the *S*-minimum of the Θ-*S* profiles in early summer along the 27.2 isopycnal highlights the pathway for mixing of AAWW across the PF through frontal mesoscale processes.

In terms of the upwelling and transformation of LCDW and UCDW, what we observe seems to be an imbalance between the continual wind-driven upwelling of LCDW and UCDW and the transformation of these water masses through mixing. The patterns of change shown in Figures 13–16 during the summer, where we observe a warming and freshening in the cold/salty LCDW and a salinification and cooling in the UCDW, most likely suggest recharge of UCDW through mechanical wind-driven upwelling, and the slight erosion of

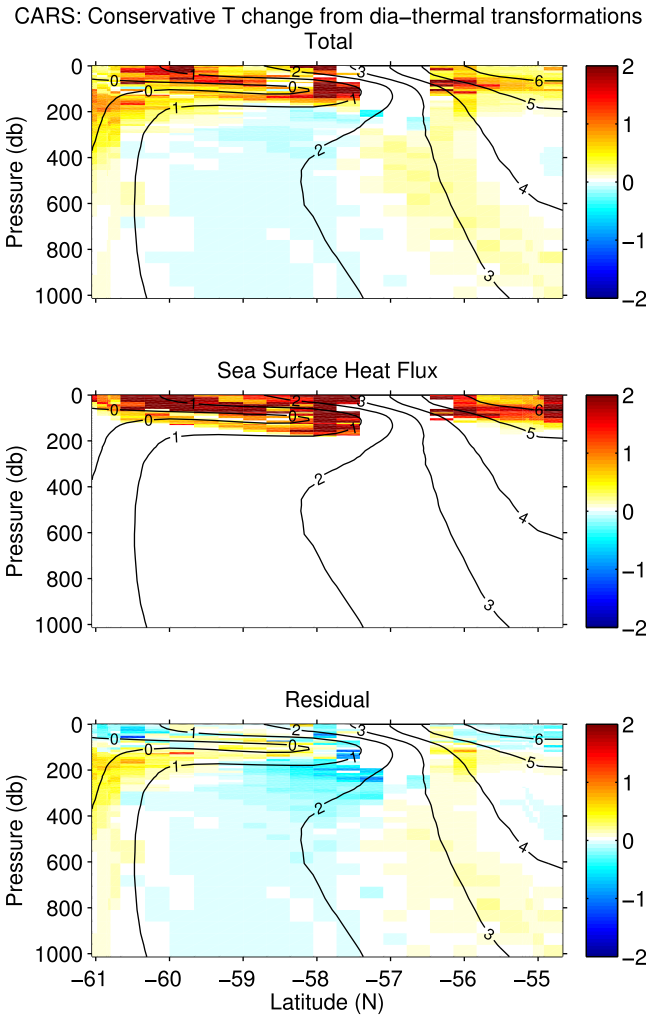
CARS: Conservative T change from dia–thermal transformations

Total

Sea Surface Heat Flux

Residual

Figure 15. (top) The implied early to late summer change in Θ calculated from the total, (middle) surface buoyancy inferred, and (bottom) residual fluxes of water mass area calculated using the CARS seasonal climatology and the WHOI air/sea flux product. Black contour lines indicate mean Θ. Units °C.

LCDW as it is mixed with the fresher UCDW. During the winter, UCDW gets fresher and slightly warmer as it mixes with AAIW and surface water, but the LDCW seems to get saltier and colder. As UCDW gets lighter during the winter, mixing between the LCDW and UCDW is reduced, so that the upwelling rate of LCDW exceeds the transformation of LCDW to lighter water masses through mixing, thus producing the apparent salinification and cooling that we observe in thermohaline coordinates.

Based on the seasonal change in water mass area of LCDW during the summer, a meridional transport anomaly of LCDW can be roughly estimated. We take the sum of the water mass area change within the region of Θ-*S* space associated with LCDW (Figure 6, far right dashed box) and multiply by an approximation of the zonal extent of LCDW. This approximation is derived by calculating the fractional area associated with LCDW according to the CARS mean state estimate (~0.2) in a zonal transect at ~57°S (the mean latitude of the SR1b section), and multiplying by the circumpolar width at this latitude (~21,400 km). This assumes that the zonal width of LCDW is much greater than the thickness. This yields a seasonal transport anomaly estimate for LCDW of approximately 10 Sv (1 Sv = 1×10^6 m^3 s^{-1}) directed southward, interpreted as a transformation of LCDW to lighter, UCDW and near-surface water. This agrees well with the similar estimate of 13 Sv by *Talley* [2013].

The above interpretation of the results presented in sections 3–6 is at this stage speculative given the limited available data and the potential for unknown changes of water mass area as a consequence of changes in the movement of water across the geographical boundary of the domain used to calculate water mass area. Changes in the meridional wind-driven upwelling of CDW, downwelling of AAIW and the zonal transport of the ACC could alias as a dia-surface transformation that may be misinterpreted above (Figure 5b). However, preliminary volumetric analysis of the entire Southern Ocean in CARS and an ocean circulation state estimate (ECCO) [*Wunsch and Heimbach*, 2013] suggests similar seasonal variations of water mass volume. An important consideration is also the sensitivity of this method to the chosen time-interval. This will depend on the accuracy and reliability of the observational data being used relative to the size of the signal in question and could be tested using a numerical model.

8. Summary and Conclusions

A method is presented to diagnose seasonal changes in water mass properties in thermohaline coordinates. The use of this coordinate system naturally removes the adiabatic effects of mesoscale variability to enable

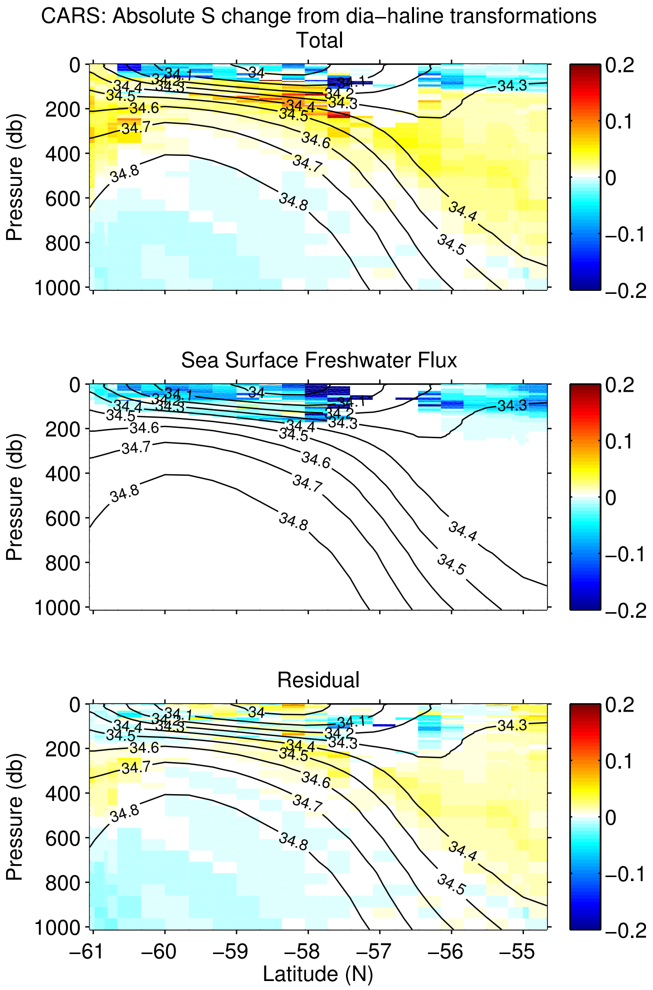

Figure 16. As in Figure 15 but showing the implied seasonal change in *S*. Black contour lines indicate mean *S*. Unit: g kg^{-1}.

a clearer interpretation of the diabatic processes that drive water mass changes. The early to late summer seasonal changes in two data sets of Θ and *S* observations were compared. The first data set comprising 20 repeat hydrographic sections along Drake Passage, the second a monthly seasonal climatology of the surface 1000 m of the ocean interpolated to the station positions used in the sections. In an Eulerian, fixed geographical coordinate system the seasonal change according to the two data sets vary due to the presence of adiabatic heaving of isopycnals by mesoscale processes in the section occupations. The main goal of this study was, therefore, to present the seasonal change in the section occupations and the seasonal climatology in a manner that is not aliased by these mesoscale processes.

Both data sets were projected into thermohaline coordinates by determining the water mass area associated with each Θ-*S* class within Θ-*S* space. The change in distribution of water mass area within Θ-*S* space from early to late summer was then used to estimate the dia-thermal and dia-haline transformation of water mass area, representing the amount of water transformed by the difference between each grid cell in Θ-*S* space to account for the redistribution of water mass area from early to late summer. The resultant change in water mass area and the inferred dia-surface transformations are similar according to both data sets. A clear redistribution of subsurface water mass area is similarly evident in both data sets including a warming of the seasonally formed AAWW, a warming and salinification of AAIW, salinification of UCDW and freshening of LCDW.

Using air/sea flux data sets of heat and E-P, the dia-surface transformation of water mass area and the resultant water mass area change were determined. For both the section occupations and the seasonal climatology, these dia-surface transformations indicate a warming and freshening of surface waters. Subtracting the water mass area change inferred using surface buoyancy fluxes from the seasonal water mass area change gives a residual water mass area change and therefore a residual dia-surface transformation. The residual water mass area change and the implied transformation highlight in particular the seasonal erosion of AAWW by diapycnal mixing given the convergent nature and nonisopycnal direction of the residual vectors.

Winter changes in water mass area distribution were also explored using the seasonal climatology. The change in water mass area from March to September and the derived dia-surface transformations show an opposing pattern of change to that observed during the summer. The determination of dia-surface transformations from air/sea fluxes is limited due to a lack of air/sea flux data during the winter especially in ice covered regions of Drake Passage.

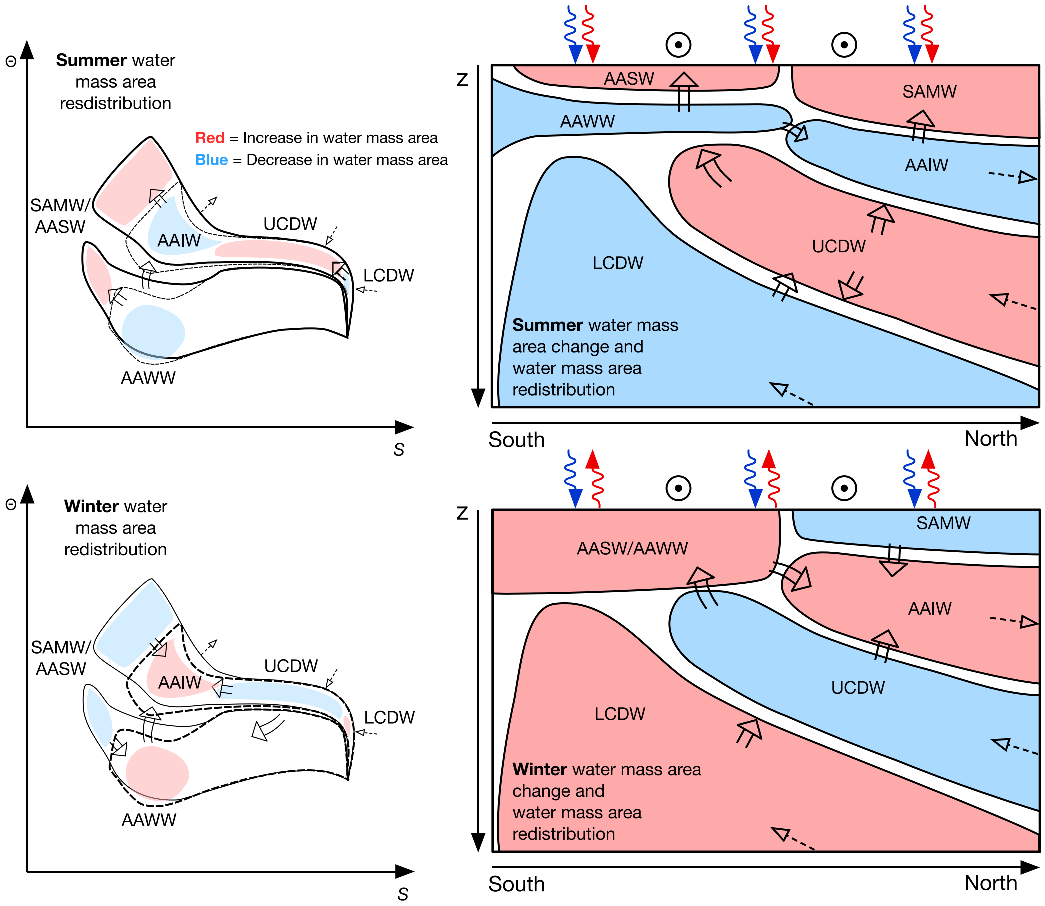

Figure 17. (top) A schematic representing the changes in the distribution of water mass area during the summer and (bottom) winter in (left) thermohaline coordinates and (depth/latitude; right) Eulerian coordinates highlighting the processes affecting the key water masses within Drake Passage. In both, the solid black arrows indicate the transformation of water mass area and the dashed black arrows represent a advection of water into and out of the geographical domain from which water mass area is calculated. The color change represents the change in water mass area (red = increase, blue = decrease). In the thermohaline coordinate schematic, the solid line and dashed lines are the summer and winter distribution of water mass area, respectively. In the Eulerian coordinate schematic, the red and blue arrows represent fluxes of heat and freshwater, respectively, in or out of the ocean and the black circles with dots represent the direction of the zonal winds out of the page.

Our analysis is consistent with the superposition of continual wind-driven overturning and seasonally variable water mass transformation. In the winter, strong surface cooling and consequent deep mixed layers form a large amount of AAWW and AAIW out of surface waters and underlying remnant AAWW and CDW. This depletes the CDW layer and increases the AAIW layer despite the likely constant inflow of CDW and outflow of AAIW. During the summer AAWW is eroded through surface warming and interior mixing and AAIW is exported. Meanwhile the CDW layer is inflated suggesting summertime wind-driven recharge in preparation for AAWW and AAIW formation the following winter.

Appendix A: NOCSv2 Water Mass Area and Flux Comparison

From the NOCSv2 air/sea flux data set, monthly mean long-wave radiation, short-wave radiation, latent heat flux, and sensible heat flux were used to calculate the net heat flux. Freshwater flux was calculated using the NOCSv2 evaporation rate and precipitation rate products. All NOCSv2 products are globally gridded to 1° for 1973–2006. Dia-surface transformation of water mass area inferred from the NOCSv2 climatology (Figure 18, top left: SR1b section occupations; top right: CARS) show a similar pattern of freshening and warming to the WHOI climatology, apart from a small positive dia-haline transformation at the warmest Θ in the CARS climatology. The residual water mass area change and dia-surface transformations determined using the NOCSv2 climatology (Figure 18, bottom left: SR1b section occupations; bottom right: CARS) are

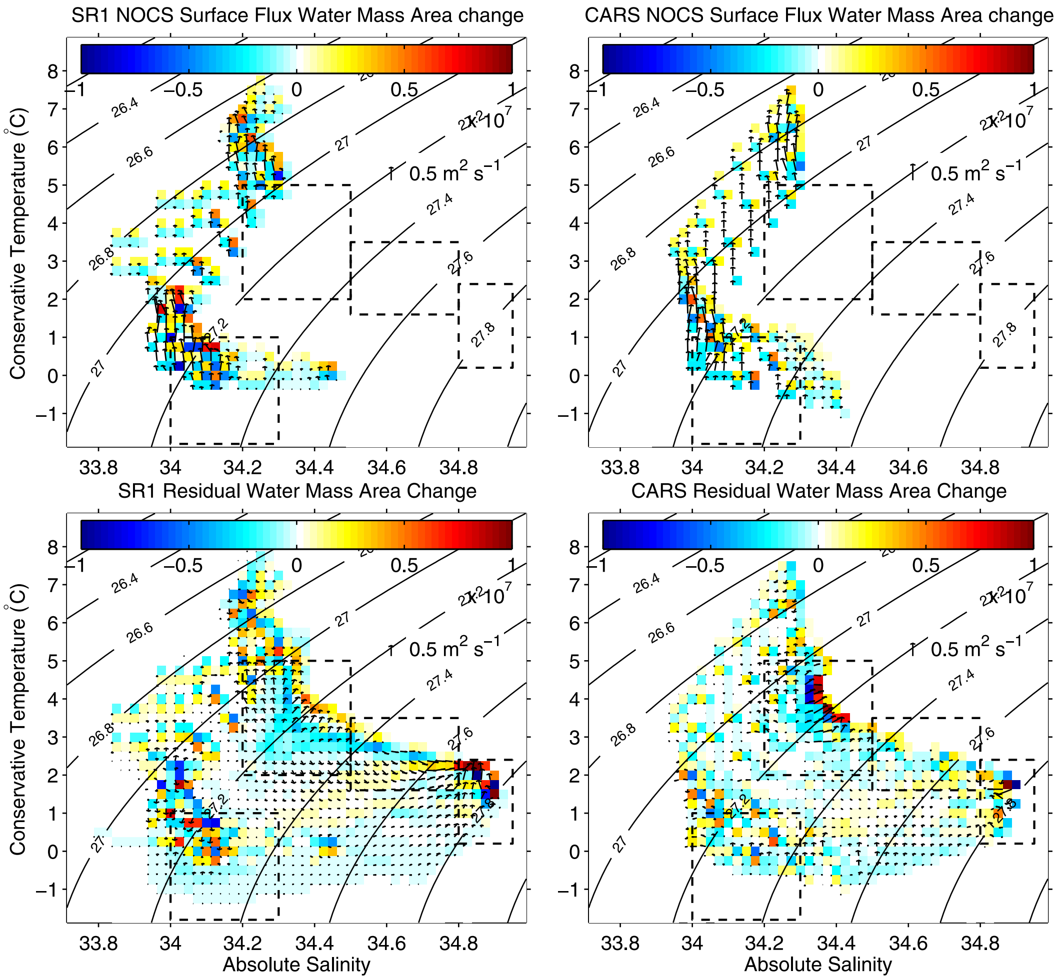

Figure 18. As in Figures 9 and 10 but showing dia-surface transformations and Θ-*S* area change inferred from (top row) the NOCSv2 surface flux climatology and (bottom row) inferred residual change for (left column) the SR1b section occupations and (right column) the CARS climatology.

therefore similar to those determined using the WHOI climatology, particularly the region of Θ-*S* space that defines the AAWW. This consistency between sea-surface flux data sets gives confidence in the reliability of both data.

Acknowledgments

SR1 section CTD data are available online from the British Oceanographic Data Centre (www.bodc.ac.uk). The CARS climatology was accessed online from www.cmar.csiro.au/cars. The WHOI OAflux data set (including ISCCP radiation data) was downloaded from the WHOI OAflux project website (http://oaflux.whoi.edu). GPCP precipitation data (version 2.2) were accessed online from http://www.gewex.org/gpcp.html. NOCS flux V2.0 data are available online through http://badc.nerc.ac.uk/data/nocs_flux. DGE was supported by a Natural Environment Research Council studentship award at the University of Southampton. JDZ was supported by a Natural Environment Research Council Postdoctoral Fellowship Award. ACNG acknowledges the support of a Phillip Leverhulme prize. We thank Bob Marsh, Gael Forget, and two anonymous reviewers for their helpful comments on earlier versions of this manuscript. We also thank the tireless and invaluable effort of those scientists, technicians, officers, and crew involved in the collection and dissemination of the CTD data used as part of this analysis.

References

Adler, R. F., et al. (2003), The version-2 global precipitation climatology project (gpcp) monthly precipitation analysis (1979-present), *J. Hydrometeorol.*, *4*(6), 1147–1167, doi:10.1175/1525-7541(2003)004<1147:TVGPCP>2.0.CO;2.

Badin, G., R. G. Williams, Z. Jing, and L. Wu (2013), Water mass transformations in the southern ocean diagnosed from observations: Contrasting effects of air-sea fluxes and diapycnal mixing, *J. Phys. Oceanogr.*, *43*(7), 1472–1484, doi:10.1175/JPO-D-12-0216.1.

Berry, D. I., and E. C. Kent (2009), A new air-sea interaction gridded dataset from ICOADS with uncertainty estimates, *Bull. Am. Meteorol. Soc.*, *90*(5), 645–656, doi:10.1175/2008BAMS2639.1.

Bindoff, N. L., and T. J. McDougall (1994), Diagnosing climate change and ocean ventilation using hydrographic data, *J. Phys. Oceanogr.*, *24*, 1137–1152.

Boning, C. W., A. Dispert, M. Visbeck, S. R. Rintoul, and F. U. Schwarzkopf (2008), The response of the Antarctic Circumpolar Current to recent climate change, *Nat. Geosci.*, *1*, 864–869.

Bryden, H. L., E. L. McDonagh, and B. A. King (2003), Changes in Ocean water mass properties: Oscillations or trends, *Science*, *300*, 2086–2088.

Cerovečki, I., L. D. Talley, and M. R. Mazloff (2011), A comparison of southern ocean air-sea buoyancy flux from an ocean state estimate with five other products, *J. Clim.*, *24*(24), 6283–6306, doi:10.1175/2011JCLI3858.1.

Chelton, D. B., M. G. Schlax, and R. M. Samelson (2011), Global observations of nonlinear mesoscale eddies, *Prog. Oceanogr.*, *91*(2), 167–216, doi:10.1016/j.pocean.2011.01.002.

Curry, R. G., M. S. McCartney, and T. M. Joyce (1998), Oceanic transport of subpolar climate signals to mid-depth subtropical waters, *Nature*, *391*, 575–577.

Curry, R., B. Dickson, and I. Yashayaev (2003), A change in the freshwater balance of the Atlantic Ocean over the past four decades, *Nature*, *426*, 826.

Delcroix, T., C. Henin, V. Porte, and P. Arkin (1996), Precipitation and sea-surface salinity in the tropical pacific ocean, *Deep Sea Res., Part I*, *43*(7), 1123–1141, doi:10.1016/0967-0637(96)00048-9.

Delcroix, T., M. J. McPhaden, A. Dessier, and Y. Gouriou (2005), Time and space scales for sea surface salinity in the tropical oceans, *Deep Sea Res., Part I*, *52*(5), 787–813, doi:10.1016/j.dsr.2004.11.012.

Döös, K., J. Nilsson, J. Nycander, L. Brodeau, and M. Ballarotta (2012), The world ocean thermohaline circulation, *J. Phys. Oceanogr.*, *42*(9), 1445–1460, doi:10.1175/JPO-D-11-0163.1.

Downes, S. M., N. L. Bindoff, and S. R. Rintoul (2009), Impacts of climate change on the subduction of mode and intermediate water masses in the southern ocean, *J. Clim.*, *23*, 6526–6541, doi:10.1175/2010JCLI3620.1.

Durack, P. J., and S. E. Wijffels (2010), Fifty year trends in global ocean salinities and their relationship to broadscale warming, *J. Clim.*, *23*, 4342–4362.

Durack, P. J., S. E. Wijffels, and R. J. Matear (2012), Ocean salinities reveal strong global water cycle intensification during 1950 to 2000, *Science*, *336*, 455–458.

Fyfe, J. C., and O. A. Saenko (2006), Simulated changes in the extratropical southern hemisphere winds and currents, *Geophys. Res. Lett.*, *33*, L06701, doi:10.1029/2005GL025332.

Grist, J. P., R. Marsh, and S. A. Josey (2009), On the relationship between the north Atlantic meridional overturning circulation and the surface-forced overturning streamfunction, *J. Clim.*, *22*(19), 4989–5002, doi:10.1175/2009JCLI2574.1.

Groeskamp, S. J., J. D. Zika, T. J. McDougall, B. M. Sloyan, and F. Laliberté (2014), The representation of ocean circulation and variability in thermodynamic coordinates, *J. Phys. Oceanogr.*, *44*, 1735–1750.

IOC, SCOR, and IAPSO (2010), The international thermodynamic equation of seawater—2010: Calculation and use of thermodynamic properties [in English], *Manuals and Guides 56*, Intergovernmental Oceanographic Commission, UNESCO.

Marshall, J., and K. Speer (2012), Closure of the meridional overturning circulation through southern ocean upwelling, *Nat. Geosci.*, *5*(3), 171–180.

Maze, G., G. Farget, M. Buckley, J. Marshall, and I. Cerovecki (2009), Using transformation and formation maps to study the role of air-sea heat fluxes in North Atlantic eighteen degree water formation, *J. Phys. Oceanogr.*, *39*, 1818–1835.

Meijers, A. J., N. L. Bindoff, and S. R. Rintoul (2011), Frontal movements and property fluxes: Contributions to heat and freshwater trends in the southern ocean, *J. Geophys. Res.*, *116*, C08024, doi:10.1029/2010JC006832.

Meredith, M. P., et al. (2011), Sustained monitoring of the southern ocean at drake passage: Past achievements and future priorities, *Rev. Geophys.*, *49*, RG4005, doi:10.1029/2010RG000348.

Naveira Garabato, A. C., D. P. Stevens, A. J. Watson, and W. Roether (2007), Short-circuiting of the overturning circulation in the Antarctic Circumpolar Current, *Nature*, *440*, 194–197, doi:10.1038/nature05832.

Naveira Garabato, A. C., L. Jullion, D. P. Stevens, K. J. Heywood, and B. A. King (2009), Variability of subantarctic mode water and Antarctic intermediate water in the drake passage during the late-twentieth and early-twenty-first centuries, *J. Clim.*, *22*(13), 3661–3688, doi: 10.1175/2009JCLI2621.1.

Nurser, A. J. G., R. Marsh, and R. G. Williams (1999), Diagnosing water mass formation from air-sea fluxes and surface mixing, *J. Phys. Oceanogr.*, *29*, 1468–1487.

Park, Y.-H., E. Charriaud, and M. Fieux (1998), Thermohaline structure of the Antarctic surface water/winter water in the Indian sector of the southern ocean, *J. Mar. Syst.*, *17*(1–4), 5–23, doi:10.1016/S0924-7963(98)00026-8.

Purkey, S. G., and G. C. Johnson (2010), Warming of global abyssal and deep southern ocean waters between the 1990s and 2000s: Contributions to global heat and sea level rise budgets, *J. Clim.*, *23*(23), 6336–6351, doi:10.1175/2010JCLI3682.1.

Ridgway, K. R., J. R. Dunn, and J. L. Wilkin (2002), Ocean interpolation by four-dimensional weighted least squares—Application to the waters around Australasia, *J. Atmos. Oceanic Technol.*, *19*(9), 1357–1375, doi:10.1175/1520-0426(2002)019<1357:OIBFDW>2.0.CO;2.

Rintoul, S. R., and A. C. Naveira-Garabato (2013), Dynamics of the southern ocean circulation, in *Ocean Circulation and Climate: A 21st Century Perspective*, 2nd ed., edited by G. Siedler et al., pp. 471–492, Academic, Oxford.

Schiffer, R. A., and W. B. Rossow (1985), ISCCP global radiance data set: A new resource for climate research, *Bull. Am. Meteorol. Soc.*, *66*(12), 1498–1505, doi:10.1175/1520-0477(1985)066<1498:IGRDSA>2.0.CO;2.

Schulz, E. W., S. A. Josey, and R. Verein (2012), First air-sea flux mooring measurements in the southern ocean, *Geophys. Res. Lett.*, *39*, L16606, doi:10.1029/2012GL052290.

Speer, K. G. (1993), Conversion among north Atlantic surface water types, *Tellus, Ser. A*, *45*, 72–79.

Speer, K. G., S. R. Rintoul, and B. M. Sloyan (2000), The diabatic Deacon cell, *J. Phys. Oceanogr.*, *30*, 3212–3222.

Talley, L. D. (1996), Antarctic Intermediate Water in the South Atlantic, in *The South Atlantic: Present and Past Circulation*, edited by G. Wefer et al., pp. 219–238, Springer, Berlin Heidelberg.

Talley, L. D. (2013), Closure of the global overturing circulation through the Indian, pacific, and southern oceans: Schematics and transports, *Oceanography*, *26*(1), 80–97.

Walin, G. (1982), On the relation between sea-surface heat flow and thermal circulation in the ocean, *Tellus*, *34*, 187–195.

Wunsch, C., and P. Heimbach (2013), Dynamically and kinematically consistent global ocean circulation state estimates with land and sea ice, in *Ocean Circulation and Climate: A 21st Century Perspective*, 2nd ed., edited by G. Siedler et al., pp. 553–579, Academic, Oxford.

Yu, L., X. Jin, and R. A. Weller (2006), Role of net surface heat flux in seasonal variations of sea surface temperature in the tropical Atlantic Ocean, *J. Clim.*, *19*(23), 6153–6169, doi:10.1175/JCLI3970.1.

Zika, J. D., B. M. Sloyan, and T. J. McDougall (2009), Diagnosing the Southern Ocean Overturning from tracer fields, *J. Phys. Oceanogr.*, *39*, 2926–2940.

Zika, J. D., M. H. England, and W. P. Sijp (2012), The ocean circulation in thermohaline coordinates, *J. Phys. Oceanogr.*, *2*, 708–724, doi: 10.1175/JPO-D-11-0139.1.